Near Surface Geophysics

EAGE
EUROPEAN
ASSOCIATION OF
GEOSCIENTISTS &
ENGINEERS

Characterization of silty to fine-sandy sediments with SH waves: full waveform inversion in comparison with other geophysical methods

Michaela Schwardt[1]*, Daniel Köhn[1], Tina Wunderlich[1], Dennis Wilken[1], Martin Seeliger[2], Thomas Schmidts[3], Helmut Brückner[4], Sait Başaran[5] and Wolfgang Rabbel[1]

[1]*Institute of Geosciences, Kiel University, Otto-Hahn-Platz 1, 24118, Kiel, Germany,* [2]*Faculty of Geosciences/Geography, Goethe University Frankfurt, Altenhöferallee 1, 60438, Frankfurt, Germany,* [3]*Römisch-Germanisches Zentralmuseum, Kompetenzbereich Antike Schifffahrt, Neutorstr. 2b, 55116, Mainz, Germany,* [4]*Institute of Geography, University of Cologne, Albertus-Magnus-Platz, 50923, Köln, Germany, and* [5]*Enez Arkeoloji Kazısı Başkanlığı, Istanbul Üniversitesi, Sosyal Tesisleri, 2270, Enez, Turkey*

ABSTRACT

We apply seismic full waveform inversion to SH- and Love-wave data for investigating the near-surface lithology at an archaeological site. We evaluate the resolution of the applied full waveform inversion algorithm through ground truthing in the form of an excavation and sediment core studies. Thereby, we investigate the benefits of full waveform inversion in comparison with other established methods of near-surface prospecting in terms of resolution capabilities and interpretation security. The study is performed in a presumed harbour area of the ancient Thracian city of Ainos. The exemplary target is the source of a linear magnetic anomaly oriented perpendicular to the coast, which was found in a previous magnetic gradiometry survey, suggesting a mole. The SH-wave full waveform inversion recovered a subsurface SH-wave velocity model with submeter resolution showing lateral and vertical velocity variation between 40 and 150 m/s. To tame the non-linearity of the full waveform inversion, a sequential inversion of frequency bands has to be combined with time-windowing in order to separate the Love wave from the reflected SH wavefield. We compare the full waveform inversion results with multichannel analysis of surface waves, standard seismic reflection imaging, electrical resistivity tomography and electromagnetic induction. It turns out that the respective depth sections are correlated to a certain degree with the full waveform inversion results. However, the structural resolution of the other geophysical methods is significantly lower than for the full waveform inversion. An exception is the reflection seismic imaging, which shows the same resolution as full waveform inversion but can only be interpreted together with the full waveform inversion–based velocity model. An archaeological excavation as well as coring data allows ground truthing and a direct understanding of the geophysical structures. The results show that the target was a sort of near-surface trench of about 3–4 m width and 0.8 m to 1.0 m depth, filled with silty sediment, which differs from the layered surrounding in colour and composition. The ground truthing revealed that only SH-wave full waveform inversion and seismic reflection imaging could image the trench and sediment structure with satisfying lateral and depth resolution. We emphasize that the velocity distribution from SH-wave full waveform inversion agrees

*E-mail: michaela.schwardt@ifg.uni-kiel.de

closely with the excavated subsurface structures, and that the discovered changes in seismic velocity correlate with changes in the sand content in the respective sediment facies sequences. The study demonstrated that SH-wave full waveform inversion is capable to image structural and lithological changes in the near subsurface at scales as low as 0.5 m, thus providing the high resolution needed for archaeological and geoarchaeological prospection.

Key words: Archaeogeophysics, Full waveform, Interpretation, Inversion, Tomography.

1 INTRODUCTION

Since the early 1980s, the theoretical base of full waveform inversion (FWI) is well established (e.g. Virieux and Operto, 2009). Only recently, first attempts were published showing that FWI has the potential to evolve into a promising tool for an improved interpretation of near-surface seismic data sets. Conventional methods, such as refraction or surface-wave seismics, have been successfully applied for solving near-surface questions for many years. However, the resolution of these methods is limited, and small-scale structures may not be resolved. In contrast, the use of the whole recorded wavefield increases the resolution significantly, indeed to its wave-theoretical limit, and allows therefore the imaging of subsurface structures smaller than the seismic wavelength in the near subsurface (Dokter *et al.*, 2017; Köhn *et al.*, 2017; 2019). Previous studies showed that the FWI approach is able to resolve small-scale near-surface structures with highest possible resolution in different fields of applications. For example, Tran and McVay (2012) developed an FWI for geotechnical site characterization, like the detection of sinkholes (Tran *et al.*, 2013), the evaluation of unknown foundations (Nguyen *et al.*, 2016) and roadway subsidence (Tran and Sperry, 2018). FWI has been further applied for hydro-geophysical site characterization (von Ketelhodt *et al.*, 2018) and in the field of tunnel investigation (Bharadwaj *et al.*, 2017). Zhang *et al.* (2019) demonstrated the application of FWI to detect tunnel lining defects and Chen *et al.* (2017) applied a combined workflow of frequency-dependent traveltime tomography and FWI to detect a known buried tunnel. A case study of detecting buried targets within the shallow subsurface in an urban set-up using traveltime inversion and FWI is presented in Alam (2019). Although many methodical developments were made, many studies are restricted to synthetic cases. Especially studies including surface-wave field data in addition to body waves are still rare. Dokter *et al.* (2017) developed an elastic SH-FWI

workflow for Love-wave data and showed an application to both synthetic and real near-surface data. Krampe *et al.* (2019) investigated the effects of anisotropy of surface waves in case of vertically transversely isotropic media. FWI in the context of archaeological exploration has been introduced only recently by Köhn *et al.* (2018; 2019).

In this paper, we investigate the applicability of FWI to exploring very near-surface targets and the possible benefits of FWI in comparison with other established methods of near-surface prospecting. In contrast to previous studies, which concentrated on tests with synthetic data, we evaluate the prospection results by ground truthing through excavation and corings.

For this purpose, we apply two different FWI workflows in a comparative way to a 2D SH-wave data set acquired to investigate the upper 5 m of the subsurface with intended 0.5 m-scale resolution such as needed for archaeological prospection. The FWI results are then compared with multichannel analysis of surface waves (MASW), seismic reflection profiling, electric resistivity tomography (ERT), electromagnetic induction (EMI) and magnetic profiling.

The test object is a suspected mole of a silted lagoon near the ancient Thracian city of Ainos, today's Enez (NW Turkey, Fig. 1a). The ancient city of Ainos is known from written sources as one of the major harbour cities of Southern Thrace. The location of its harbours is still unknown, though. Therefore, the site has been investigated in the past years by archaeological and geophysical surveys, part of which serve here for comparison with FWI. The investigation target was originally detected in a magnetic gradiometry survey and, in the beginning, suspected to represent the remnants of an ancient harbour construction (Fig. 1b).

The swampy riparian environment of the test target consists of fine-grained sediments water-saturated until close to the surface. To explore this setting seismically, we applied horizontally polarized shear waves (SH waves and Love waves)
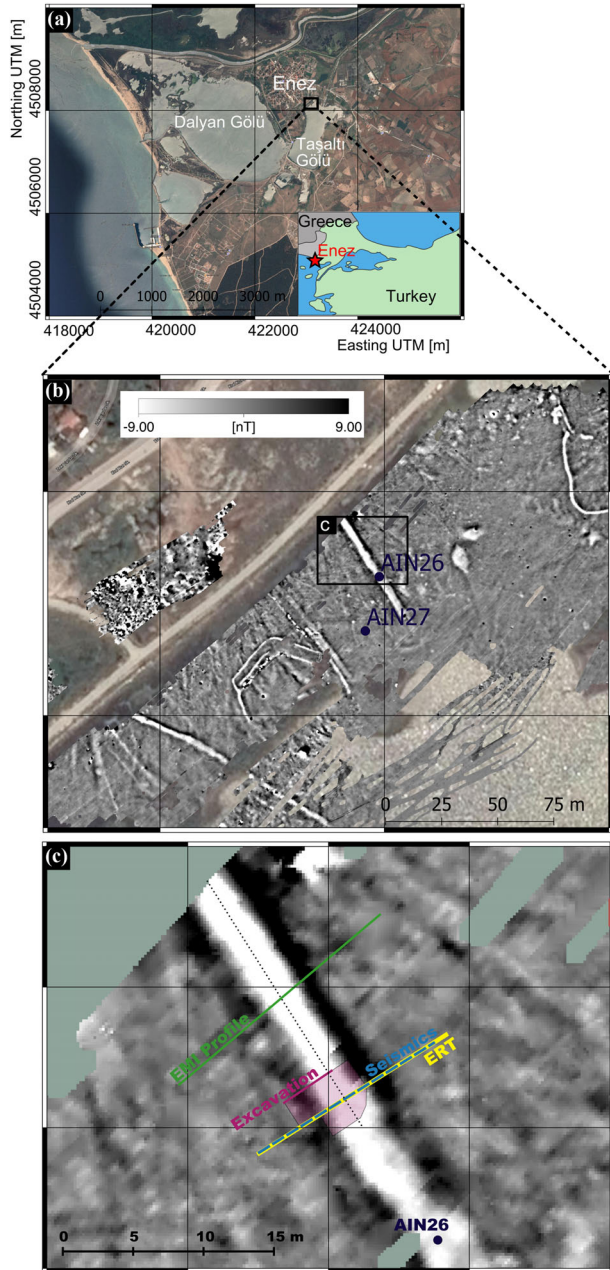
Figure 1 (a) Map of the research area (source: Google Satellite). (b) Close-up of the investigated area with the magnetic anomaly map in grey colours and the location of the sediment cores Ain26 and Ain27. (c) Investigated magnetic anomaly with positions of geophysical profiles, sediment core Ain26 and excavation. Coordinates in UTM Zone 35N, WGS 84.

because the influence of water saturation on SH-wave velocity is almost neglectable. Therefore, in contrast to P waves, SH waves are not affected in structural resolution and lithological sensitivity by the water table.

The basic objectives of this paper are threefold:

1. To investigate the increase in resolution and reliability of shear-wave sounding by the application of FWI in comparison with MASW and standard reflection imaging using the example of an archaeological site with apparently minor lithological variation. The results are validated by corings and excavation. Since FWI results depend, to a certain extent, on details of the workflow, we test two different workflows in this context.

2. To investigate along the same line the benefit in resolution and interpretation security gained by applying SH-wave FWI in comparison with standard non-seismic methods of near-surface prospecting.

3. As a by-product, we clarify the origin of a magnetic anomaly serving as target in this methodical study and put it in an archaeological context, thereby demonstrating the advantage of an integrative multi-method prospection approach.

We first give an introduction to the archaeological and geological setting, the general concept and details of the applied geophysical measurements followed by a results section and a discussion corresponding to the three objectives above.

2 GEOLOGICAL AND ARCHAEOLOGICAL SETTING AND HISTORICAL CONTEXT

The settlement area of the ancient city of Ainos (modern: Enez) is located in the westernmost part of Turkish Thrace, in direct vicinity to the mouth of the Hebros river (Greek: *Evros*; Turkish: *Meriç*). It debouches into the Aegean Sea, creating an extensive deltaic floodplain north of the Turkish city of Enez (Fig. 1a). The lower course of the Hebros forms the border between modern Greece and Turkey. Surrounded by the Taşaltı Gölü lagoon to the south, the Dalyan Gölü lagoon to the west and the southernmost branch of the river Hebros to its north, Ainos is situated on a limestone headland. The Dalyan Gölü is separated from the Aegean Sea by a complex barrier beach system. The environs of Ainos are characterized by swampy marshes and small coastal lakes; the water supply is controlled by rainfall and the channel flow of the Hebros (Flemming, 1978; Başaran, 2001; Anzidei *et al.*, 2011; Seeliger *et al.*, 2017; Seeliger *et al.*, 2018).

Brückner *et al.* (2015) analysed an 11 m long coring (Ain5) in the area of the Taşaltı Gölü lagoon and determined radiocarbon ages of near-surface strata from it. The existence of a shallow lagoonal water body can be inferred from the fourth millennium BC up to nearly modern times which is backed by the dating of an articulated *Cerastoderma glaucum* (C.g.) at a depth of 4.64 m below sea level (b.s.l.) to 3664–3348 calibrated (cal) BC and a further one at 1.15 m b.s.l.

to cal AD 1416–1665. Shortly after sediment input led to a silting up of the area. During this process, a short phase of littoral conditions due to the migration of the shoreline occurred. Coarser grain size and low ratios of Ca/Fe and Ca/K back this interpretation (Brückner *et al.*, 2015).

Due to its position close to the mouth of the river Hebros, Ainos was an important traffic hub from seventh century BC to the 15th century AD containing different harbour locations of different purposes. Unfortunately, the question of the location of those harbours is not answered conclusively. One harbour was proposed on the eastern shore of the Dalyan Gölü, where Byzantine fortifications are preserved and masonry further in the south had been interpreted as the remains of a former breakwater (Başaran, 1999). Recent investigations including geophysical as well as geoarchaeological prospection were undertaken since 2012 to detect potential ancient and Byzantine harbour structures (Brückner *et al.*, 2015; Rabbel *et al.*, 2015a). Following an initial magnetic survey, attempts were made to identify the cause of a linear magnetic anomaly by coring and by depth resolving geophysical methods typically applied in archaeological prospecting (ground-penetrating radar, electromagnetic induction and electrical resistivity tomography). However, the latter were affected by the low electrical resistivity values of the fine-grained, saltwater-saturated lagoonal sediments.

3 CONCEPT OF GEOPHYSICAL MEASUREMENTS

For more than 60 years, magnetometry has been used for archaeological prospection (Belshé, 1957; Aitken, 1958). Several applications and case studies mapped walls, stone foundations and other archaeological remains like pottery (e.g. Gibson, 1986; Larson *et al.*, 2003). Examples of the application of magnetometry to the detection of ancient harbour structures are present in Boyce *et al.* (2004), Rabbel *et al.* (2004) and Paoletti *et al.* (2005). Being the basic method in archaeological prospection (Neubauer, 2001), magnetic gradiometry surveying was applied first to obtain an overview map of the study area which is limited to the coastal area of the Taşaltı Gölü lagoon close to the city of Enez, being the most probable area for an ancient harbour in this lagoon. This survey revealed magnetic anomalies that were tentatively interpreted as remains of ancient harbour construction. However, test corings did not show evidence of solid construction material.

In many cases, it is useful or even necessary to supplement magnetics with other methods such as ground-penetrating radar (GPR), electric resistivity tomography (ERT) or electro-

magnetic induction (EMI) measurements (Larson *et al.*, 2003; Keay *et al.*, 2009; Rabbel *et al.*, 2015b). The multi-sensory approach, that is, the combination of different measurement methods with different sensors, for the investigation of an archaeological target defines the state of the art in research and allows a more accurate interpretation of anomalies while reducing ambiguity (Rabbel and Müller-Karpe, 2004; Leucci *et al.*, 2007; Mohamed *et al.*, 2019). Therefore, one of these magnetic structures was investigated using 2D ERT and EMI.

ERT and electromagnetic prospection have both been used in archaeological prospection for over 30 years. They have successfully been applied to a large number of sites for mapping buried targets (Papadopoulos *et al.*, 2006) like remnants of walls or buildings (e.g. Dogan and Papamarinopoulos, 2003; Rizzo *et al.*, 2005) as well as a medieval farmstead and a palaeoriver system (De Smedt *et al.*, 2013). De Smedt *et al.* (2014) showed that EMI is sensitive to vertical soil variation and also able to detect weak magnetic anomalies. Bonsall *et al.* (2013) showed that EMI is able to detect a wide range of archaeological features like ditches or pits. Examples of the application to harbour structures are stated in Wunderlich *et al.* (2018), where the extent and shape of a harbour basin was determined by ERT profiling and in Vafidis *et al.* (2005), where wall remnants could be mapped.

Since these methods show only limited structural resolution, GPR was applied in addition. GPR has been used in archaeological prospection since the 1970s. Examples in archaeological prospection are numerous: burial tombs (Goodman and Nishimura, 1993), historic cellars (Bevan and Kenyon, 1975) and buried walls (Vickers and Dolphin, 1975) have successfully been located. However, the GPR measurements applied in the lagoon of Ainos suffered from electromagnetic absorption caused by the very low electrical resistivity of the lagoon sediments, which restricted depth penetration of the electromagnetic waves to less than 0.5 m.

Finally, a multi-fold covered seismic profile was acquired using horizontally polarized shear waves (SH waves). Seismic reflection and refraction measurements using shear waves were successfully applied in archaeological prospection occasionally, for example for the reconstruction of silted up harbour basins or waterways (e.g. Stümpel *et al.*, 1988; Rabbel *et al.*, 2004; Woelz and Rabbel, 2005; Woelz *et al.*, 2009; Wilken *et al.*, 2015a). The use of surface waves appears attractive in onshore archaeological prospecting because of their large amplitudes and high sensitivity to the SH-wave velocity and because targets are so shallow that they are still in the depth range of metre-scale surface wavelengths (Wilken *et al.*, 2015b; Wunderlich *et al.*, 2015; Dokter *et al.*, 2017).

In the water-saturated sediments of lagoonal environments, SH waves propagate at much lower velocities than the usually applied compressional (P-waves), thus enabling structural resolution of the order of 1.0 m or even below. The seismic records, which show basically SH-body waves and Love waves, were evaluated using FWI and compared with the results of multichannel analysis of surface waves of Love waves as well as conventional reflection seismic processing.

4 DATA ACQUISITION AND STANDARD PROCESSING METHODS

An overview of the applied field instruments, acquisition parameters and other specifications is given for all methods in Table A.1 in Appendix A. Table A.2 in Appendix A gives information about the physical parameters measured with each method and petrophysical links. All profiles were positioned perpendicularly to the magnetic anomaly with the anomaly being at the centre and ensuring that adequate non-anomalous regions were covered. The length of each profile was chosen to ensure sufficient depth of penetration, and a point spacing was selected to ensure appropriate resolution of the near surface.

4.1 Magnetic prospection

For the magnetic measurements, we used an array of six fluxgate gradiometers mounted on a handcart (for acquisition details see Appendix A, Table A.1). Positioning was done using a real-time kinematic differential global positioning system (RTK-DGPS), which yields an accuracy of 0.01–0.02 m. In addition, an array of two fluxgate sensors was mounted on a frame in front of a boat to conduct offshore measurements in shallow water. The mean of the measured data is subtracted from the data measured by each sensor for every profile followed by an interpolation of the whole data set onto a 0.2 m × 0.2 m grid.

The spatial sampling of the magnetic gradiometer survey is 0.05 m in-line, assuming a measurement speed of 1 m/s with a sampling rate of 20 Hz, and 0.5 m crossline, corresponding to the sensor spacing. Due to the limitations of potential field theory, magnetic measurements are principally highly ambiguous in depth resolution.

4.2 Seismic data acquisition

We acquired one seismic profile perpendicular to the magnetic anomaly (Fig. 1c; for acquisition details see Table A.1).

We excited SH waves by horizontal hammer blows against a steel plate. The steel plate was coupled to the ground by steel spikes at its bottom. The seismic signals were recorded with horizontal-component 10-Hz geophones. Hammer blows and horizontal-component sensors were oriented perpendicular to the profile direction. The seismic signal-to-noise ratio (S/N) depends on both the shot position and the receiver offset. The noise level is calculated as variance of the amplitude before the first breaks, the signal is determined as variance of the amplitudes after the first breaks. Generally, it can be said that for shot-receiver offsets smaller than 3.25 m, it is S/N > 30 and for offsets larger than 11.0 m it is S/N < 5. Medium offsets between 3.25 and 9.0 m have an average S/N of 12.

4.3 Seismic reflection processing

For conventional seismic reflection processing, the data have been trace normalized and corrected for geometrical spreading. In addition, automatic gain control (AGC) with a window length of 0.05 s was applied. The dominant surface waves are suppressed using an *f–k* filter. Afterwards, the AGC was reversed. A bandpass filter with cut-off frequencies of 10 and 150 Hz was applied to eliminate high-frequency noise. The data were sorted into common midpoint (CMP) gathers. A velocity analysis using coherency-based velocity spectra (Neidel and Tanner, 1971) showed that optimum stacking results could be obtained by applying an averaged 1D NMO-velocity function. A semblance filter was applied to smooth the resulting CMP-stacked section. Then the data were migrated using Stolt migration with the stacking velocity. Afterwards, the section was converted to a depth section applying the same velocity as for migration.

For conventional seismic reflection measurements, the maximum spatial resolution is about one-quarter of the dominant wavelength. With a centre frequency of approximately 60 Hz and a mean velocity of 100 m/s, the vertical as well as the horizontal resolution of the migrated section are 0.4 m, which is confirmed by the migrated reflection image.

4.4 Multichannel analysis of surface waves

The multichannel analysis of surface waves (MASW; e.g. Socco *et al.*, 2010) is used to obtain information about the 2D shear-wave velocity structure based on the dispersion of Love waves. We follow the approach presented in Bohlen *et al.* (2004) and Wilken and Rabbel (2012) (for details see Appendix B).

Phase-slowness frequency *(p–f)* spectra are calculated for local wavefields of the first shot at moving centre points. Four exemplary spectra are given in Fig. B.1 (Appendix B). Dispersion curves are identified and fitted by forward modelling. We use the adapted particle swarm optimization of Wilken and Rabbel (2012) to minimize the misfit between observed and modelled dispersion curves, to obtain velocity models for each centre point position. A detailed description of the parameters and inversion workflow is given in Appendix B.

The horizontal resolution of MASW is given by the width of the Fresnel zone. The depth of penetration of surface waves depends on the frequency: lower frequencies penetrate deeper whereas higher frequencies have a low penetration depth. In general, the depth of penetration is about one half of the dominant wavelength, the latter being approximately 2.5 m.

4.5 Electromagnetic induction

We conducted electromagnetic induction (EMI) measurements along a profile perpendicular to the magnetic anomaly (for acquisition details see Table A.1; Fig. 1c) using a CMD MiniExplorer with coil distances of 0.32 m, 0.71 m and 1.18 m, measured in both horizontal coplanar (HCP) and vertical coplanar (VCP) mode. Examples of the raw data and their respective standard deviations are given in Fig. C.1 (Appendix C). As all data points and conductivity values exhibit only very small errors (less than 1%), no further processing was necessary. We performed a conductivity inversion using the IX1Dv3 software by Interpex. The profile was inverted using a homogeneous initial model (2040 mS/m, based on the initial model for ERT) using the *smooth model estimation* option with Occam's inversion. The inversion algorithm searches for the smoothest model possible fitting the data within a tolerance instead of only minimizing the data fit, which would result in a rough model (Constable *et al.*, 1987). Further details about the inversion can be found in Appendix D.1.

The point spacing along the profile determines the spatial horizontal resolution for the EMI survey, which is 1.0 m and was chosen based on the width of the previously measured magnetic anomaly. The effective depth ranges vary with the coil spacing and amount to 0.5, 1.0 and 1.8 m for HCP mode and to 0.2, 0.5 and 0.9 m for VCP mode for the three spacings used, respectively. The skin depth is approximately 2.4 m, based on the measured conductivity values.

4.6 Electric resistivity tomography

We measured an ERT profile perpendicular to the considered suspicious linear magnetic anomaly using both Wenner-alpha and dipole–dipole configuration (Fig. 1c; for acquisition details see Table A.1). The Wenner-alpha configuration is characterized by a high vertical resolution with a horizontally stratified subsurface and a low lateral resolution in contrast to the dipole–dipole configuration, which has a better lateral resolution but a lower depth of penetration. Examples of the raw data and their respective standard deviations are given in Fig. C.1 (Appendix C). The inversion of the data was carried out using the software package BERT (boundless electrical resistivity tomography; Günther *et al.*, 2006) with a homogeneous initial model of 0.5 Ωm, which corresponds to the mean value of all measured points. Data points with a standard deviation larger than 5 % were excluded from the inversion and deleted. A regularization parameter of $\lambda = 54$ was applied in the inversion, which was selected based on the L-curve method (Hansen and O'Leary, 1993). A more detailed description of the inversion algorithm is found in Appendix D.2. In order to investigate the reliability of the obtained model, the depth of investigation (DOI) was calculated following the approach of Oldenburg and Li (1999). For the DOI study we used two different homogeneous initial models (0.2 Ωm and 200 Ωm, respectively). The obtained DOI value is less than 0.001.

The spatial resolution of ERT measurements depends on the electrode configuration, electrode spacing as well as on the depth of the structures. Additionally, the electric conductivity has a significant influence on the resolution. The depth of penetration also depends on the electrode spacing, the total profile length and conductivity. As a rule of thumb, one can assume that the depth of penetration of an electrode spread is about one-quarter to one-half of the separation between the current electrodes for Wenner-alpha and the same fraction of the distance between the current and potential dipoles for the dipole–dipole configuration (Lange and Jacobs, 2005). The largest electrode spacing is 5.25 m, the largest dipole spacing is 1.5 m, resulting in a penetration depth of approximately 1.3 to 2.6 m for Wenner-alpha and 0.4 to 0.8 m for dipole–dipole configuration, respectively.

4.7 Magnetic modelling

To compare the magnetic data with the results of the other methods, we extracted magnetic amplitudes from the gridded areal data along a line parallel to the seismic profile. From the seismic results, two alternative subsurface structures with

polygonal cross sections were derived and the corresponding susceptibility contrasts were determined by modelling according to the method of Talwani and Heirtzler (1964). Important parameters needed for the calculation of the total field T are the inclination I, declination D and azimuth C of the earth magnetic field at the survey location along with the magnetic induction $\mathbf{B}$. Furthermore, we need to consider that the fluxgate magnetometers measure the vertical distance of the vertical component only, as well as the magnetometer height above the ground and the sensor spacing. Details of the models and parameters are stated in Table A.3, and details about the calculation and inversion of the susceptibility are found in Appendix D.3.

5 2D-SH SEISMIC FULL WAVEFORM INVERSION

The seismic full waveform inversion (FWI) aims at the derivation of a high-resolution model of elastic parameters of the subsurface. By including all information of the seismic record (i.e. seismic phases and amplitudes) in the inversion, the FWI is capable to resolve structures below the seismic wavelength (e.g. Köhn *et al.*, 2014). In this study, the FWI is based on minimizing the following objective function:

$$E = -\sum_{i=1}^{ns} \int_0^T \mathrm{d}t \sum_{j=1}^{nr} \left[\frac{u_{ij}^{\mathrm{mod}}(t)\, u_{ij}^{\mathrm{obs}}(t)}{\|u_{ij}^{\mathrm{mod}}(t)\|_2 \|u_{ij}^{\mathrm{obs}}(t)\|_2} \right], \qquad (1)$$

where ns and nr are the number of sources and receivers and T is the recording time. u_{ij}^{mod} and u_{ij}^{obs} are the modelled and measured data, respectively. Equation (1) is called the global correlation norm (GCN). More details of the used FWI approach and the properties of the GCN are discussed in Appendix E.

5.1 General workflow

The general workflow of the FWI consists of four parts:

(1) Pre-processing of the data,
(2) Estimation of the initial model,
(3) Selection of the optimum inversion strategy,
(4) FWI.

Steps (1)–(3) are discussed in detail in the following section (see also flowchart in Fig. 2), with the main focus on the inversion strategy. The basic concept and equations of the applied FWI algorithm are described in Appendix E.

5.1.1 Pre-processing of seismic data

The acquired seismic data cover a frequency band from 10 to 150 Hz. Due to the high signal-to-noise ratio (S/N), the data are well suited for the application of the FWI, and only a small amount of pre-processing is required. Within each shot gather, the seismic traces are normalized to the maximum amplitude of the gather. Following Forbriger *et al.* (2014), a time-dependent spreading correction is applied to each shot gather to compensate 3D point source and geometrical spreading effects, which cannot be appropriately modelled by the 2D SH approximation used within the FWI code. Offset-dependent spreading effects are compensated during the inversion by using the approach of Forbriger *et al.* (2014) and Schäfer (2014). Figure 3 shows the shot gathers of three exemplary shots, the dominant Love wave, the direct wave as well as several reflections are highlighted. To enhance the visibility of the reflections, an AGC with a window length of 0.05 s is applied to the raw data. However, no AGC was applied during the FWI.

5.1.2 Initial model estimation and model discretization

Due to the local gradient-based optimization approach, the choice of the initial model m_0 is an important factor influencing the result of the FWI. The initial model is parameterized on a uniformly spaced 2D spatial Cartesian grid for every model parameter consisting of 280×280 grid points with a grid spacing of 0.05 m. The time step dt is set to 8.5×10^{-5} s to guarantee numerical stability. The grid is surrounded by an absorbing frame of perfectly matched layers (PMLs) at the bottom, left and right boundaries. The PML thickness is set to 10 grid points (0.5 m). In order to accurately model the Love-wave propagation, a free surface boundary condition is assumed at the top boundary.

The subsurface model comprises SH-wave velocity, density and Q_{SH} model. In all inversion runs, we used a constant-velocity half-space as initial SH-wave velocity model. To find an optimum initial model, this constant initial velocity was varied between 60 and 100 m/s in separate test runs. These values cover the range of velocity values found by evaluating first breaks and reflection hyperbolae. The SH-wave velocity was updated during the FWI, while the density was always left at a constant value (1800 kg/m³) because it is known to vary only little and has therefore only a minor influence on the trace-normalized seismic wavefield. In shallow sediments, viscoelastic absorption has a certain influence on the shape of the waveforms. We considered this effect by assuming a constant quality factor Q_{SH} in forward and adjoint modelling.
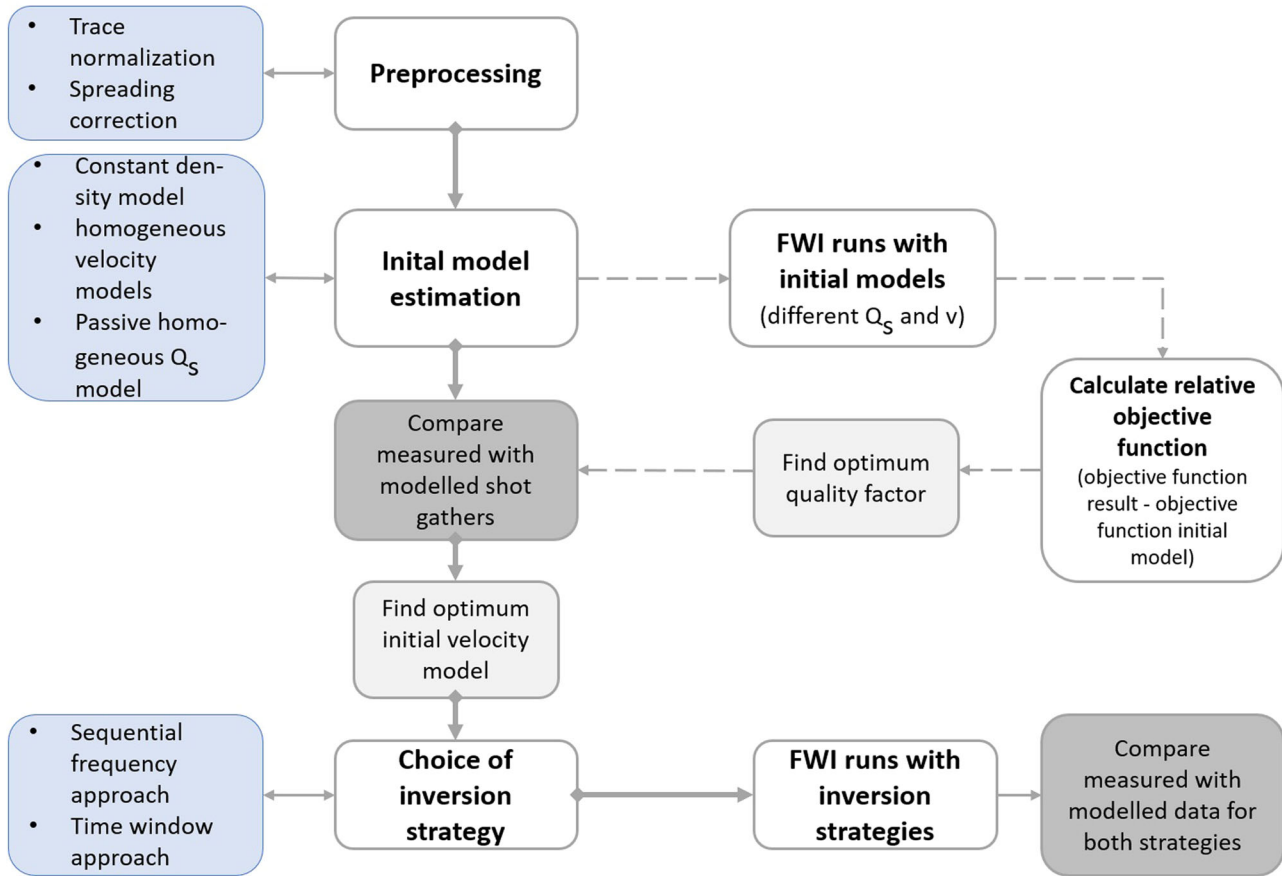
Figure 2 Illustration of the processing steps and concept of initial model estimation for the applied FWI (own compilation).

However, Q_{SH} was not updated during the FWI. Instead, we followed the approach of Dokter *et al.* (2017). It consists of determining an optimum Q_{SH} by repeating the inversion for a set of constant Q_{SH} values and using the relative objective function (value objective function result E minus value objective function initial model E_0) to select the optimum Q_{SH}. In this way, quality factor values of $Q_{SH} = 2.3, 5, 10, 15, 25, 50, 75$ were tested. The evaluation of the relative objective function yielded an optimum quality factor of $Q_{SH} = 10$.

The quality of the different initial models is evaluated by comparing the measured data with synthetic shot gathers calculated for the initial models. The optimum result was obtained for a homogeneous viscoelastic half-space model with an SH-wave velocity of $v_{SH} = 100$ m/s, a density of $\rho = 1800$ kg/m³ and a quality factor of $Q_{SH} = 10$.

The seismograms of the initial model show only the direct SH-wave arrival, which can fit the data only to a certain extent (Fig. 4). Due to the homogeneous elastic model, no Love wave

is predicted by the synthetic data. The remaining data misfit will be fitted by the FWI.

5.1.3 Inversion strategies

The FWI strategy is a key factor for a successful inversion. It needs carefully to be chosen in order to reduce the non-linearity of the inverse problem and depends on the given problem and data. In order to investigate the optimum inversion strategy for the given problem, we tested two different workflows. The results of both approaches are compared in this study.

5.1.3.1 Sequential frequency approach. The dispersion and oscillatory character of the surface wave introduces a significant non-linearity to the inversion problem. To reduce this effect, a sequential frequency approach is applied according to Dokter *et al.* (2017). The time-domain data are inverted by applying a low-pass filter with gradually increasing maximum corner frequencies of 10, 15, 30, 60, 100 and 150 Hz to the
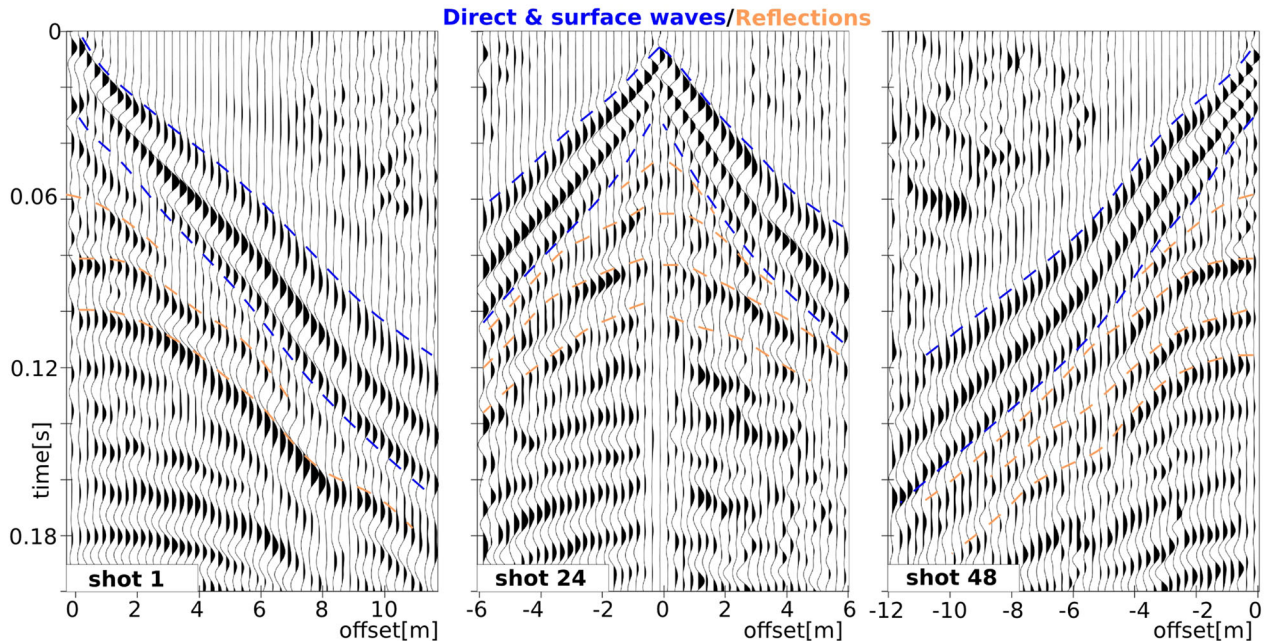
Figure 3 Examples of SH shot gathers of the spreading corrected, trace-normalized and bandpass-filtered (10–150 Hz) data for shots 1, 24 and 48. Marked with blue dashed lines are the direct and surface waves, reflections are marked with orange dashed lines. To improve the visibility of the reflections, an AGC with 50 ms window length is applied.

field data. The FWI result for each frequency band is the initial model for the next. The source wavelet is estimated at the beginning of each frequency range. Only traces within 2.2 m offset are used for the source wavelet estimation to avoid the inversion of Love-wave dispersion into the source wavelet.

5.1.3.2 Time window approach. Although much smaller in amplitude than the Love wave, the distinct reflections in the recorded data impose additional problems to the inverse problem. Especially when inverting low frequencies, the FWI can interpret the reflections as part of the Love-wave dispersion. Therefore, the Love wavefield and the reflections need to be separated and the FWI strategy must be modified accordingly. The time window FWI approach consists of two steps. In step 1, a time window is introduced in order to invert only the Love wavefield without the reflections. All reflections in the field and modelled data after the Love waveform are damped by an exponential function $e^{-\alpha(t-t_{love})}$ with a damping factor $\alpha = 1e4\ 1/s$. t_{love} denotes the end of the dominant first arrival Love waveform picked for each trace. Therefore, the time window does not affect the FWI of the Love waveform. The time windowed data are inverted using six low-pass-filtered frequency bands with gradually increasing maximum corner frequencies of 10, 15, 30, 60, 100 and 150 Hz, respectively.

Because the reflections are excluded when applying the time window FWI inversion in step 1, a second sequential

frequency inversion step starting from the time window FWI result was added, where the whole reflected and Love wavefield is inverted without a time window. The same low-pass filter strategy with the same corner frequencies is used as in step 1.

6 GEOLOGICAL, ARCHAEOLOGICAL AND GEOARCHAEOLOGICAL FIELDWORK

Several sediment cores were drilled in the study area to further investigate the subsurface source of the magnetic anomaly, focusing on cores Ain26 and Ain27 in the following (Table A.4; Fig. 1b). The cores are described according to grain size as well as colour (Munsell Soil Color Charts; Sponagel 2005) and samples for laboratory analyses were taken. An archaeological section perpendicular to the magnetic anomaly has been excavated down to a depth of 2.0 m, of which one profile will be discussed in this study.

6.1 Sedimentology and geochemistry of core samples

Multi-proxy laboratory analyses were conducted (Ernst, 1970; Engel *et al.*, 2009; Seeliger *et al.*, 2013). Samples were air-dried, ground with mortar and pestle, and sieved to separate the ≤2 mm grain-size fraction for further analyses
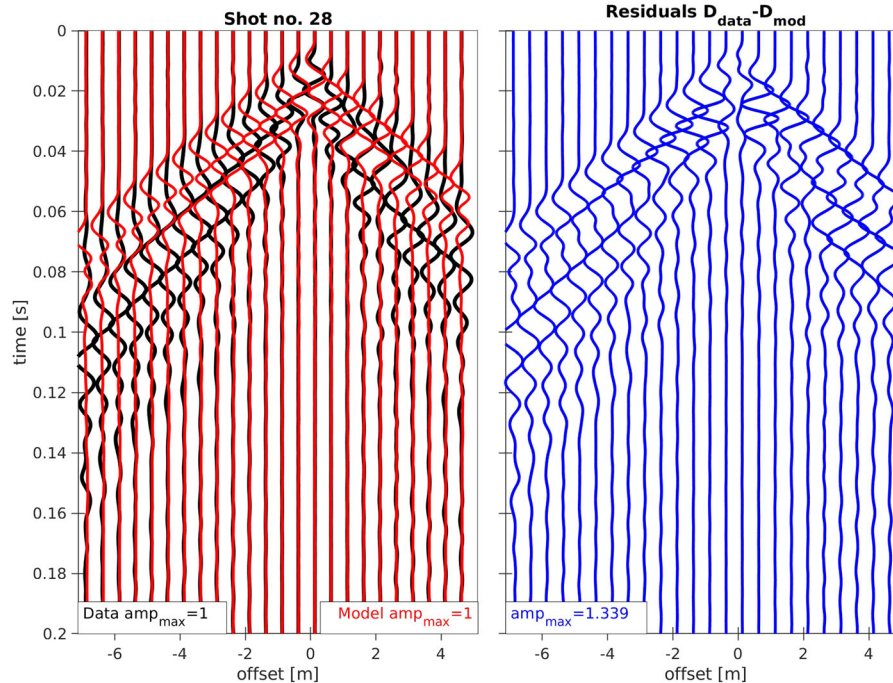
Figure 4 Comparison of observed data for shot no. 28 (black traces) with modelled data (red traces) for the best-fitting initial model. Only every second trace is shown for a better overall view. Left: Trace normalized and bandpass filtered (10–150 Hz) observed and modelled data. Right: Residuals between observed and modelled data. Values for maximum amplitude are given.

(Table A.4). The organic content was decomposed using 15% hydrogen peroxide (H_2O_2); sodium pyrophosphate ($Na_4P_2O_7$; concentration: 47 g/l) was taken as a dispersant, followed by laser-based grain-size analysis. Grain-size parameters were calculated after Folk and Ward (1957). Up to 30 elements were determined by using a portable XRF. To ensure comparability within all XRF analyses and to reduce grain-size dependence, each sample was ground to powder in a ball triturator and afterwards pressed to pills before being measured (Table A.4). The bulk-mineralogical composition was determined by X-ray diffractometry (XRD) on powder compounds using a step interval of 0.05° and a dwell time of 4 s. A fixed 1° divergence and anti-scatter slit was used at diffraction angles from 5 to 75° 2Θ. The Cu K-alpha radiation source was operated at 40 keV and 40 mA (Table A.4).

7 RESULTS

7.1 Magnetic prospection

The magnetic anomaly map shows several distinct linear anomalies in the range of ± 10 nT running from the shore to shallow water (Fig. 1b). Since the central parts of the anomalies are negative, it can be inferred that the susceptibility values

of the objects causing these linear anomalies are smaller than that of the surrounding material.

7.2 Seismics

In Fig. 5, the seismograms of the observed and modelled data for the full waveform inversion (FWI) results are shown for three exemplary shots (first, centre, last) for both the sequential frequency and time window strategy. It can be seen that near offsets are fitted equally well by both applied strategies, differences only occur for offsets larger than 4–5 m. The direct wave as well as the Love wave and its dispersion are fitted well by both modelled data sets, but later parts of the seismogram, especially the deeper reflections are not fitted well.

Both best-fitting seismic SH-wave velocity models obtained by the two applied FWI strategies display a graben-like low-velocity (50–70 m/s) zone in the uppermost first metre, being mostly similar in shape and size to each other (Fig. 6b,c, label **A**). The deepest point of this low-velocity zone is located at the same position as the magnetic minimum, marked by a dashed black line (Fig. 6a). It is underlain by a layer of higher velocities, ranging from 70 to 80 m/s in the time window approach model and of about 100 m/s in the sequential frequency approach model. In total, the velocity varies between
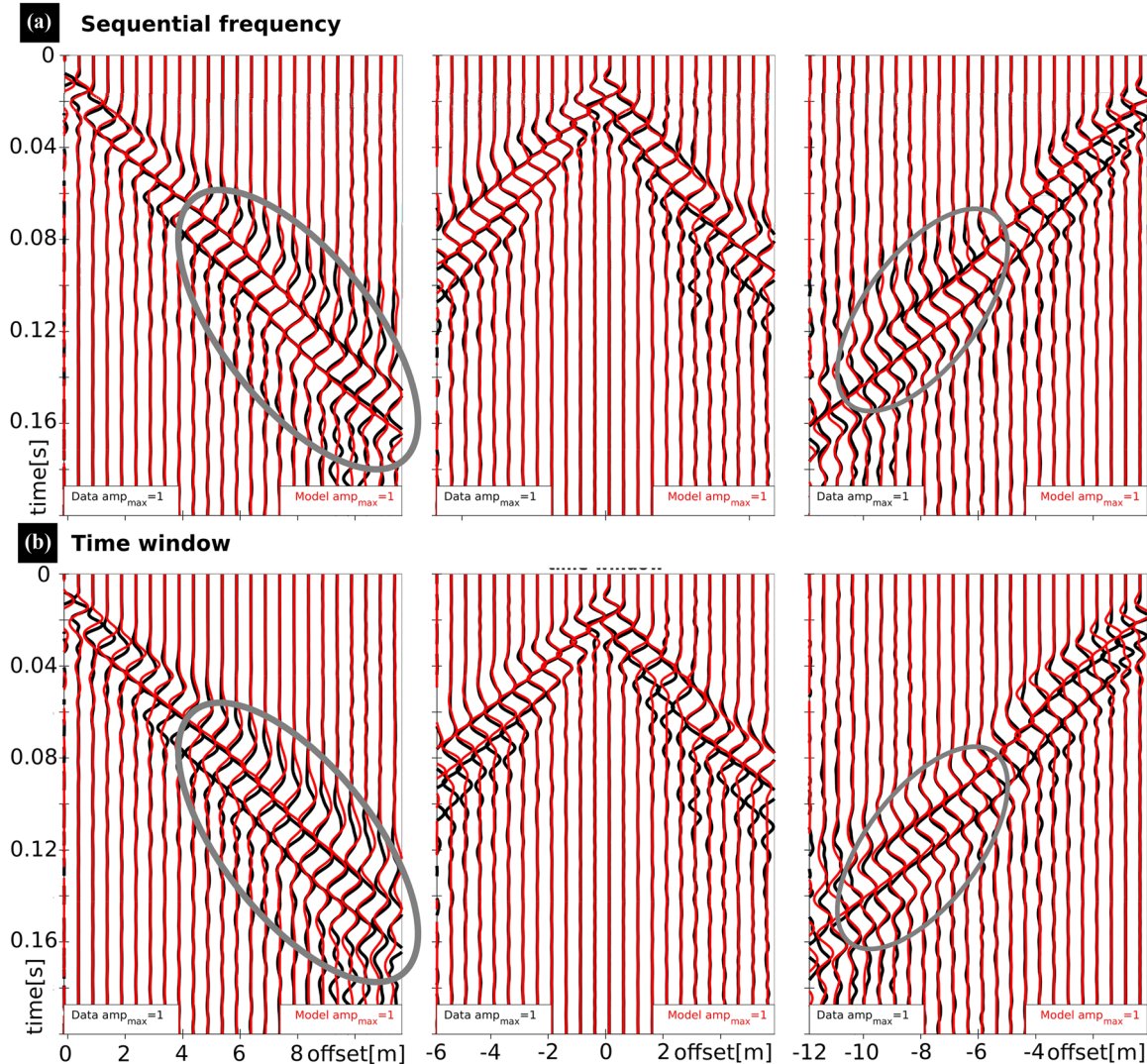
Figure 5 Comparison of three exemplary shot gathers for both tested inversion strategies. Observed data are in black, and modelled data in red. Forward modelled shot gathers for shot nos. 1, 24 and 48 for (a) the sequential frequency strategy velocity model and (b) the velocity model of the time window strategy. Only every second trace is shown; all traces are trace normalized and bandpass filtered between 10 and 150 Hz. Values for maximum amplitude are given.

40 and 160 m/s in both models. In deeper parts, the velocity models derived from the different FWI strategies differ from each other. The velocity model obtained with the time window approach shows alternating layers of high and low seismic velocities to greater depths down to approximately 9.0 m, whereas no distinct structures are visible in the deeper part of the sequential frequency approach model. Between −4.0 and −2.0 m along the profile (Fig. 6b,c, label **B**) in a depth up to 1.0 m below the surface, a high-velocity zone is located in both velocity models, displaying velocities of up to 130–150 m/s.

The velocity of the model obtained by multichannel analysis of surface waves (MASW) ranges from 65 to 170 m/s (Fig. 6d). A 5.0 m wide high-velocity zone is found in a depth between 0.5 m and 1.0 m west of the central magnetic anomaly. It is underlain by lower velocities, further decreasing to the eastern part of the profile. The topmost layer shows a relatively homogeneous velocity distribution, with the lowest overall values in the east.

The stacked seismic reflection section (Fig. 7) shows several reflectors down to a depth of 9.0 m. In a depth of 0.5 m, a strong horizontal reflector is visible, which is disrupted
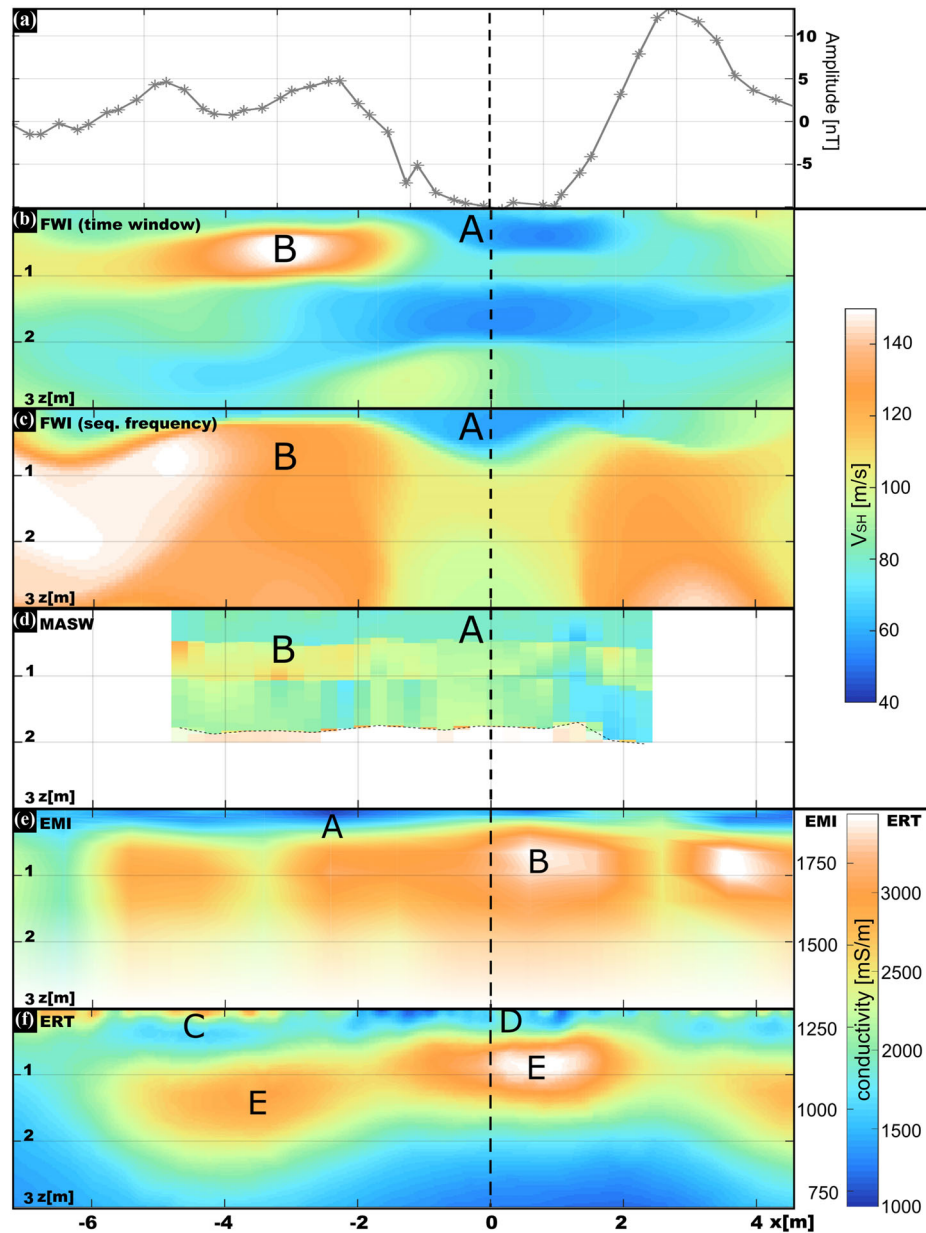
Figure 6 All profile-wise results: (a) Magnetic anomaly along the seismic/ERT line. (b) Resulting velocity model of the FWI with the time window strategy. (c) Resulting velocity model of the FWI with the sequential frequency strategy. (d) Velocity model of the MASW. (e) Conductivity depth profile obtained from the inversion of EMI with the half-space shown in transparent colours. The EMI profile is projected onto the seismic profile. (f) Conductivity depth profile obtained from ERT. The centre of the magnetic anomaly is marked by a black dashed line; capital letters A–E mark different regions of interest.

around the central magnetic anomaly between −2.0 and 2.0 m. At this position, a reflector of similar amplitude is found in a depth of 1.0 m. In the deeper part, some strong reflections are observed, e.g. in a depth of 4.0–6.5 m. There is an excellent agreement between the reflection seismic image and the velocity structure obtained by the FWI time window approach.

7.3 Electric resistivity tomography and electromagnetic induction

The direct comparison between electric resistivity tomography (ERT) and electromagnetic induction (EMI) shows that both methods yield a similar trend in the result concerning electrical conductivities (Fig. 6e,f). In the inverted EMI
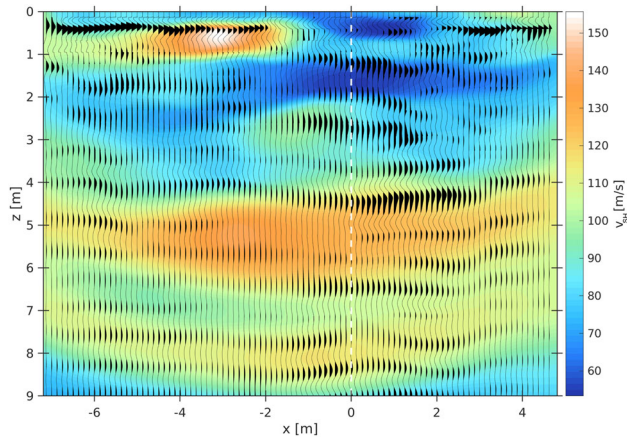
Figure 7 CMP-stacked and migrated section of the acquired seismic data, shown as black wiggle traces. The data are trace normalized, corrected for spreading and bandpass filtered between 10 and 150 Hz. The surface waves are removed using a *f–k* filter. The traces are again normalized after stacking. Travel times are converted to depths after migration using the stacking/migration velocity. The migrated section is compared with the obtained velocity model from the FWI time window approach shown in colours.

conductivity model (rms: 3.8%), the uppermost layer **A** shows homogeneous low (800–1000 mS/m) conductivities at the top underlain by increasing conductivities up to 2000 mS/m. The highest conductivity values of 1600 to 2000 mS/m can again be found in the central region of the magnetic anomaly (Fig. 6a,e, **B**). The inverted ERT profile (rms: 5.4%) shows the same basic structure as the EMI profile, although the obtained conductivities are about twice as high. The ERT model shows more details and contrast in layering than the EMI model. The topmost 0.3 m shows intermediate conductivities (2000–3000 mS/m, **C**), which are interrupted by the lowest values of 1400 mS/m at ± 2.0 m around the central magnetic anomaly (Fig. 6f, **D**). The topmost layer is underlain by lower conductivities (1500–2000 mS/m) to a depth of 0.8 m, followed by a good conducting layer **E** with values of 3000–3500 mS/m of about 1.0 m thickness.

7.4 Archaeological and geoarchaeological results

The geophysical results are compared with two sediment cores [maximal depth: 5.0 m b.s. (below surface)] as well as an archaeological section in order to ground truth the results. Indeed, we find correlations between the cores and the results of the FWI described below.

7.4.1 Corings Ain26 and Ain27

Sediment core Ain26 (final depth: 5.0 m b.s.) is situated in the centre of the magnetic anomaly (Fig. 1b,c). Sedimentologically, the profile is subdivided into three units (Fig. 8a).

The uppermost unit 3 until 0.80 m b.s. represents the contemporary appearance of a swampy, intertidal zone, influenced by the tides and fluctuating water levels caused by agricultural irrigation measures. The unit is made of very poorly sorted, fine-grained brown loamy silts (mean grain size: 17–30 μm) and contains small pieces of roots, pebbles, wood and charcoal. Ca/Fe and Ca/K ratios rise towards the surface from 0.95 to 1.6 and 0.7 to 1.4, respectively.

The underlying unit 2 (0.80–1.05 m b.s.) consists of light grey better sorted sands (mean grain size: 268 μm) and includes shell debris, seagrass fibres and small well-rounded pebbles up to 1 cm in size. Ca/Fe and Ca/K ratios are at a low level (0.7–0.75) and represents littoral conditions. Between the final depths of the core and 1.05 m b.s., the lowermost unit 1 was reached. It is made of grey, poorly sorted homogeneous clayey silts (mean grain size: 7–23 μm) and shows maxima in Ca/Fe (2.5) and Ca/K (2.1) ratios. It represents a very calm depositional environment expressed in the fine grain size and the poor sorting. High values of Ca/Fe document that the influence of the sea is visible, while high Ca/K ratios represent a quite strong influence of saltwater in contrast to freshwater. The grain-size distribution of core Ain26 (Fig. 8a) shows a peak in sand content at about 1.0 m b.s.

Basically, the same units are present in core Ain27, which was taken outside the anomaly (Figs 1b and 8b). The depths and thicknesses of units 2 and 3 differ slightly.

7.4.2 Archaeological excavation

As a final structural verification, a 5.5 m wide and 2.0 m deep trench was excavated crossing the western part of the magnetic anomaly (Fig. 1c). In the excavated section, two stratigraphic layers were identified (Fig. 9).

The dark brown topsoil is characterized by a clayey-sandy texture and contains modern finds in a ca. 0.5–0.6 m thick horizontal layer. Below the dark brown topsoil, a dark grey to black and clayey-sandy layer was identified without any archaeological artefacts.

In the western part of the excavation trench, the topsoil layer is only ca. 0.4 m thick and extends up to ca. 0.8 m in the eastern direction at the centre line of the anomaly. The pattern of strata is marked by a white line in Fig. 9. It is also marked in the seismic velocity sections from both FWI strategies and
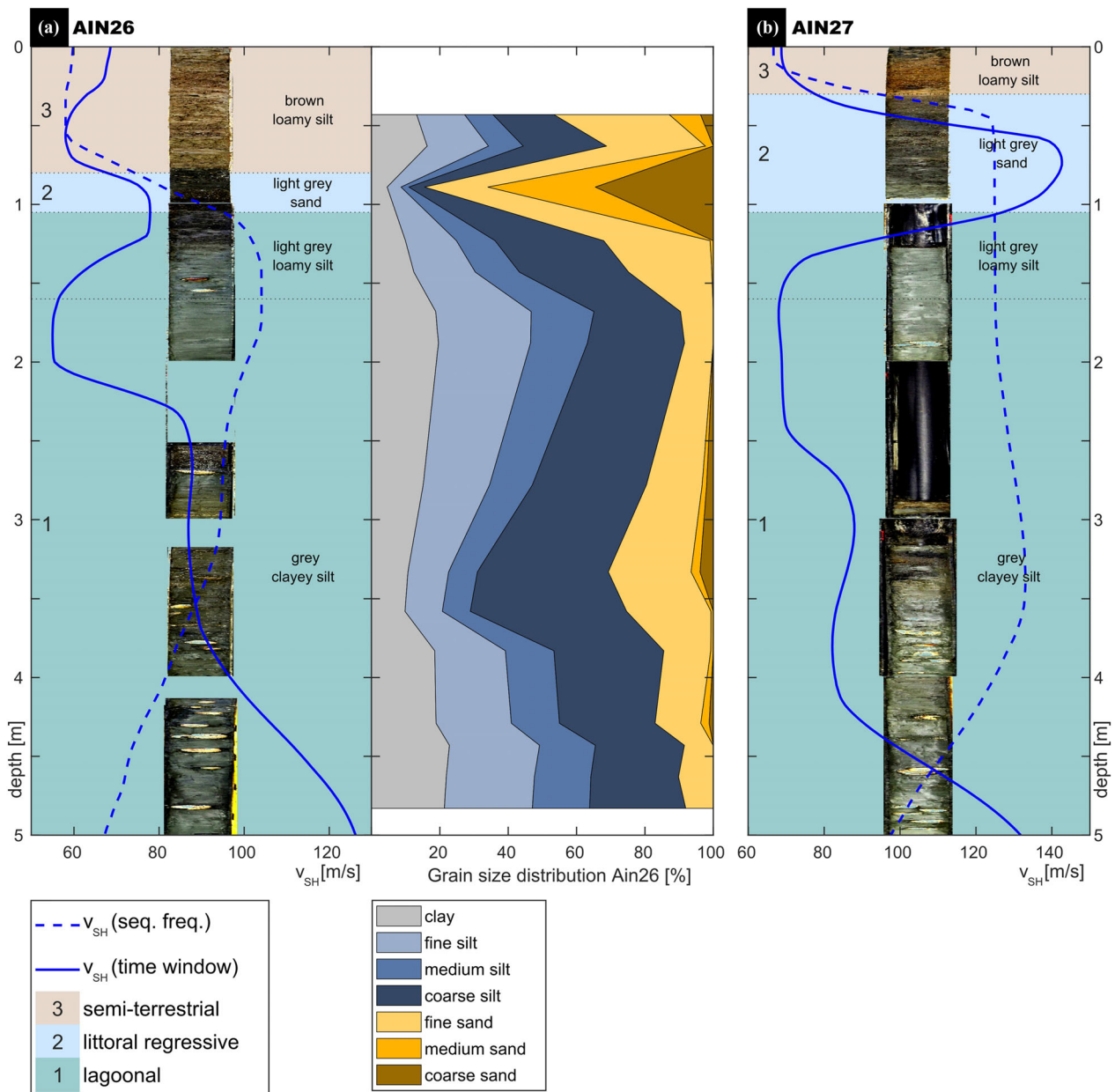
Figure 8 (a) Stratigraphic log and grain-size distribution of core Ain26 (inside the magnetic anomaly). (b) Stratigraphic log of core Ain27 (outside the magnetic anomaly). The plots also show the comparison of the velocity-depth profiles of both FWI approaches with the sediment cores down to a final depth of 5 m. The solid blue line represents the velocity of the time window approach model; the blue dashed line represents the velocity of the sequential frequency-only approach model.

MASW as well as into the conductivity models by ERT and EMI for a better comparison.

7.5 Magnetic modelling constrained by seismic structure

The aim of magnetic modelling was to verify if the magnetic anomaly could be explained by the seismic models.

The magnetic profile is modelled perpendicular to bodies extracted from the seismic velocity models obtained by both FWI strategies. The edge of the body is chosen equivalent to the isoline of a seismic velocity of 75 m/s, approximately corresponding to the layer boundary found in the excavation (Fig. 10). The susceptibility contrast between the bodies and the surrounding subsurface has been determined by inversion.
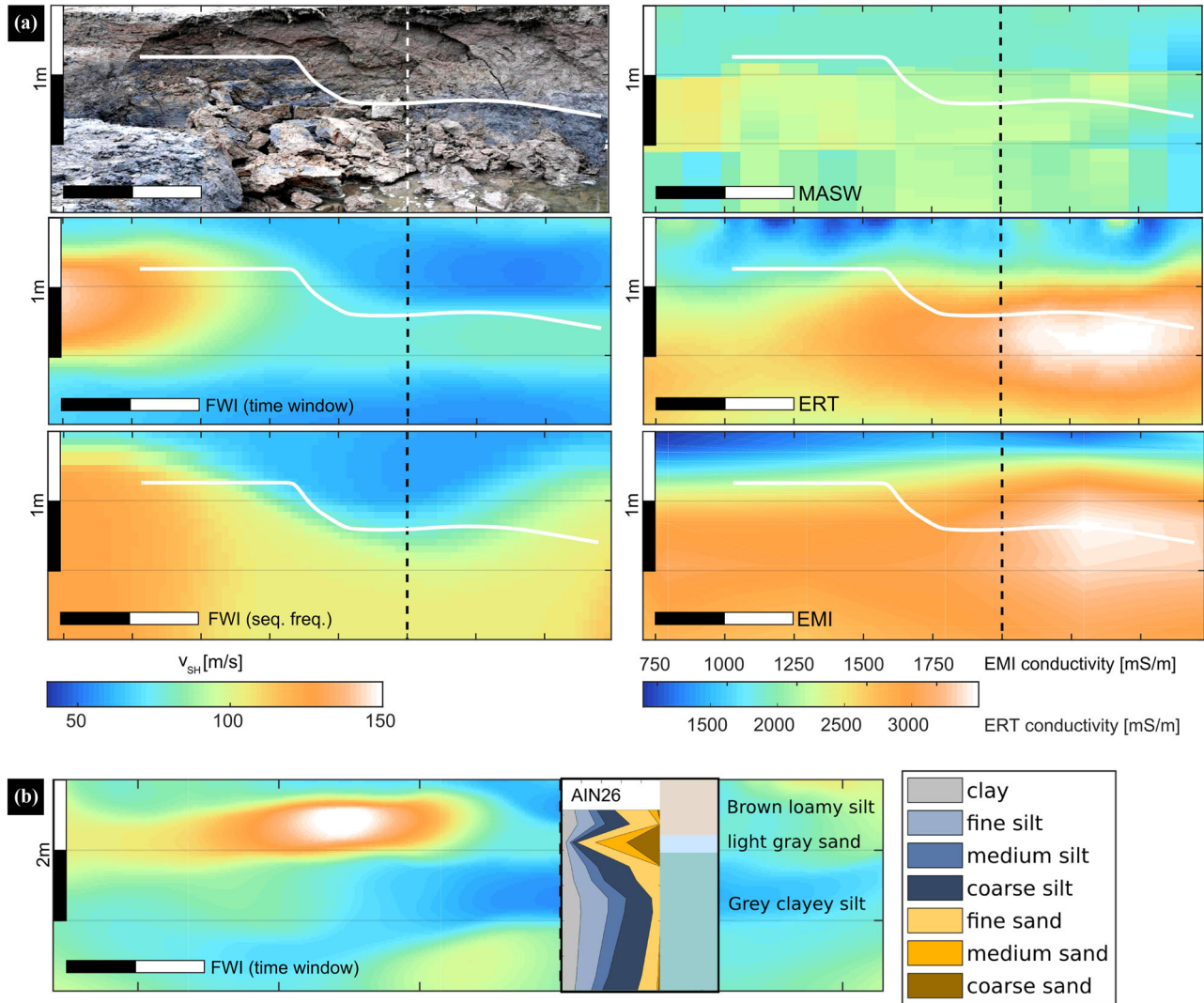
Figure 9 Comparison of the profile-wise geophysical results with the archaeological profile. (a) Photo of the archaeological profile and the corresponding parts of the geophysical results. The white solid line indicates the transition from brown to grey sediments and is transferred to all geophysical models. Vertical dashed lines at 0 m show the centre of the magnetic anomaly. (b) Sedimentological units and grain-size distribution of core Ain26 in direct comparison with the FWI time window approach result.

The best-fitting anomaly models are obtained for a difference in magnetic susceptibility of -630 and -670×10^{-5} SI between the body and the surrounding subsurface for the time window approach and the sequential frequency approach, respectively (Fig. 10). The rms is 2.3 nT for the time window approach and 2.4 nT for the sequential frequency approach, respectively.

The modelled contrasts in susceptibility are compared with laboratory measurements of samples taken at the excavated section and with samples of drilling cores Ain26 and Ain27. Both laboratory measurements of the drilling cores and the excavation show strong fluctuations in susceptibility

inside and outside of the anomalous region. Nevertheless, the changes are in the range of the modelled susceptibility contrast, which proves it to be plausible.

8 DISCUSSION

In this paper, different geophysical methods were applied to investigate a shallow archaeological structure in a swampy environment. Especially, two inversion strategies for a seismic full waveform inversion (FWI) were applied to a near-surface SH data set. The results of all applied geophysical methods
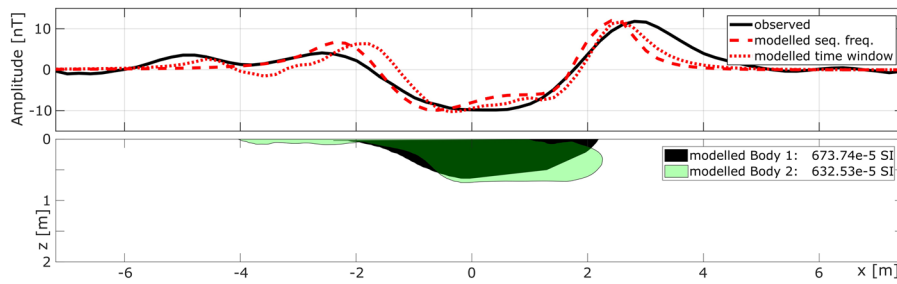
Figure 10 Result of the magnetic modelling. Top: Comparison between observed (solid black) and modelled (dashed/dotted red) magnetic data along the seismic profile for the structures shown below. The structures are extracted from the seismic velocity models; the black body is extracted from the sequential frequency approach (body 1; dashed lines in top panel); green body is extracted from the time window strategy result (body 2; dotted lines in the top panel).

show a near-surface anomaly in the region of the central magnetic anomaly (Fig. 6). This anomalous region is characterized by a negative magnetic amplitude, high specific electrical conductivities and a low seismic velocity zone in the upper 1.0 m. The geophysical results are compared with two sediment cores drilled down to a maximal depth of 5.0 m b.s. as well as an archaeological section in order to ground truth the results. Indeed, we find correlations between the cores, and the results of the FWI are described below.

In order to quantify the similarity between the geophysical results, the correlation coefficients (Fig. 11) and the normalized cross correlation are calculated for trend-corrected data $d\mathbf{A}(x, z)$. The trend $\mathbf{T}(x, z)$ for each model is calculated by eq. (2) and then subtracted from the model data $\mathbf{A}(x, z)$:

$$\mathbf{T}(x, z) = b_0 + b_1 x + b_2 xz,$$
$$d\mathbf{A}(x, z) = \mathbf{A}(x, z) - \mathbf{T}(x, z). \tag{2}$$

The normalized cross correlation is a measure of similarity and is used in pattern recognition as well as it can help to quantify lateral and vertical shifts between the models. We cross-correlated each resulting trend-corrected profile. The results of this similarity and correlation analysis are described below. In the following subsections, the results are discussed with respect to the aims of this study, evaluating the inversion strategy of the applied FWI algorithm, validating the results by ground truthing through an archaeological excavation and sediment cores, and comparing both the standard seismic and non-seismic results with the results obtained by FWI in terms of resolution.

8.1 Inversion strategy

The choice of the inversion strategy is important in order to achieve an appropriate fit of the data. A common strategy to mitigate the non-linearity of the inverse problem is a se-

quential inversion of frequency filtered data (e.g. Groos *et al.*, 2014; 2017). Usually, the data are either low or bandpass filtered during inversion within different frequency bands (Pan *et al.*, 2017; Köhn *et al.*, 2019). As suggested in previous near-surface applications (e.g. Bunks *et al.*, 1995; Dokter *et al.*, 2017), we first applied a low-pass sequential frequency filter approach. This approach was able to image the upper first 1.0 m with an adequate resolution as the comparison with the excavation showed. Deeper structures were not imaged due to the dominant Love wave, which limits the resolution when applying the sequential frequency approach. Additionally, the distinct reflections impose further problems to the inverse problem. The FWI can interpret these reflections as part of the dispersive Love wavefield. To increase the impact of the deeper reflections on the inversion result, we applied a time window strategy.

Altogether, the time window strategy yields smaller residuals, and hence a better fit of the modelled data, than the inversion without the application of a time window. The value of the global correlation norm of the resulting model obtained by the time window strategy is much lower (-3.8×10^{-5}) compared with the global misfit of the sequential frequency approach (-3.3×10^{-3}). The velocity models of both strategies are comparable for the near surface and only differ in greater depths where some reflections could be better fitted by the inversion using the time window strategy.

We compare velocity-depth profiles of both applied inversion strategies with the sediment cores. Unit 3 of core Ain26 is characterized by low seismic velocities of about 60 m/s, which increase to 80 m/s in unit 2 and the transition zone to unit 1 (blue lines in Fig. 8a). No clear velocity-lithology trend can be seen in the lowermost unit 1. The change from littoral regressive to lagoonal lithology is marked by a change from grey to light grey sediment and a decrease in velocity to 60 m/s. From 2.0 m b.s. to the final depth of 5.0 m b.s.,
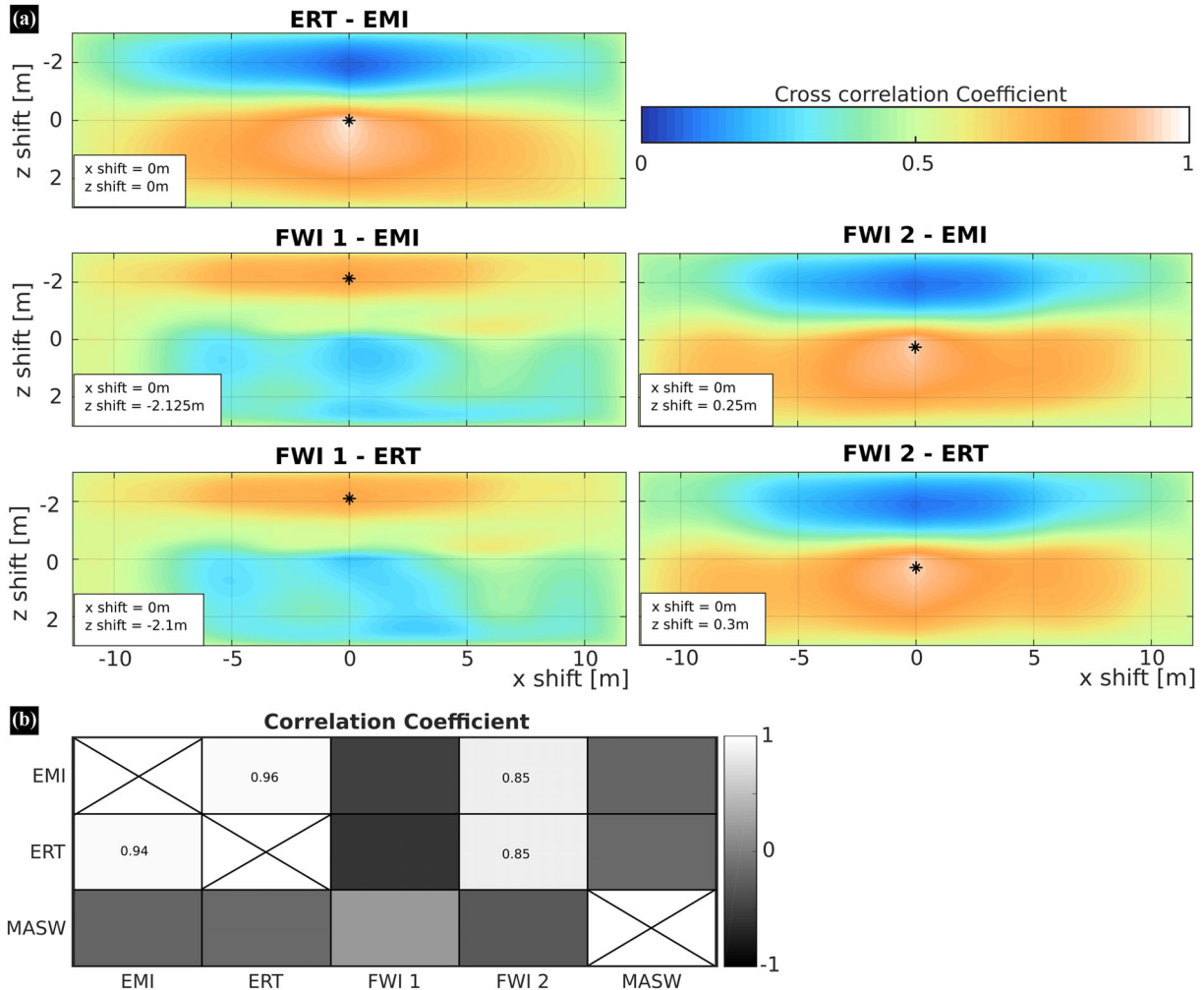
Figure 11 Calculated normalized cross correlation coefficients between trend-corrected time window strategy FWI and EMI and ERT. Vertical and horizontal axes depict vertical and horizontal shifts, respectively. Blue values correspond to a cross correlation coefficient of 0, and white values correspond to a cross correlation coefficient of 1. Black asterisks mark the maximum cross correlation coefficient. The shift values of the maximum cross correlation are given.

the velocity increases again to values larger than 120 m/s. For core Ain27 (Fig. 8b), the velocity-depth profile shows a strong increase from 70 to 130 m/s at about 0.3 m b.s., accompanied by a change in colour from brown to grey. This is followed by a decrease in velocity to 70 m/s at circa 1.0 m b.s. and a change from grey to light grey. From roughly 2.5 m b.s. to the final depth, the velocity structure is similar to that compared with Ain26 showing an increase in velocity to values of 120 m/s and higher. The velocity profiles of the sequential frequency-only approach show the same behaviour to a depth of 1.0–1.5 m b.s., but then differences and no clear correlation with the cores are apparent.

The direct comparison of the grain-size distribution with the seismic velocity (time window strategy) shows that the

maximum sand content correlates well with the maximum in seismic velocity at a depth of 0.8 m. The lower velocities directly above and below can also be correlated to the lowered sand and correspondingly increased silt/clay contents. This is in general agreement with laboratory findings of the correlation of shear-wave velocity and grain size (e.g. Schön, 2015).

Looking at the archaeological excavation (Fig. 9), it is obvious that, compared with the velocity models by FWI, in both cases the pattern of strata corresponds to the transition from low to higher velocities, but a better fit is seen for the time window strategy velocity model. While in this model the excavated structure matches the velocity structure over the full range, in the sequential frequency strategy velocity

model, the pattern of strata does only fit left of the magnetic anomaly minimum.

Although both strategies yield a comparable result for the near surface, in comparison with the excavated trench and the corings, the velocity model of the time window strategy shows the best resemblance with the subsurface structures. Therefore, as the time window strategy workflow yields the best correlation with the true subsurface and the smallest overall data residuals, it is chosen as the most probable result.

8.2 Performance of full waveform inversion in comparison with other seismic methods

Evaluating the performance of the FWI with respect to multichannel analysis of surface waves (MASW), the resulting velocity model of the time window strategy was compared with the velocity model obtained by MASW. Several distinct velocity features visible in the FWI model can be partly found in the MASW velocity model. The high-velocity zone in 0.5–1.0 m depth matches the structure seen in the FWI model in its extent and position. The low-velocity graben found by FWI at the minimum of the magnetic anomaly displays higher velocities than the FWI sections and is not shown as clearly. The velocity model obtained by MASW shows a greater similarity to the velocity model obtained by the time window approach than with the sequential frequency approach model. In comparison with the excavation, the model obtained by MASW does not show a correlation with the excavated structure. Regarding the model's depth extent, the FWI shows resolvable structures to greater depths (approximately 8.0 m), whereas the MASW only yields a model of the very near surface (upper 2.0 m). The general velocity trends are similar in the FWI and MASW models, but the low velocity zone of the investigation target is not as prominent in the MASW as in the FWI model. This is caused by the smoothing and the local 1D forward modelling applied in the MASW. Especially the local 1D approximation leads obviously to an oversimplification of real conditions. Using local wavefields and spectra, one can obtain a pseudo 2D model as the one obtained here, but at the expense of resolution which is dependent on the length of the geophone spread (Forbriger, 2003). Although the MASW is able to reconstruct a velocity model of the upper subsurface with a nominal resolution below 1.0 m (Socco *et al.*, 2010; Wunderlich *et al.*, 2018), the deeper part of the model has to be interpreted with care as the resolution decreases with depth. The standard deviations for the layer boundaries are high, varying between 10% and 36% with a mean of 20%. Figure 12 shows the layer boundaries of the average model

(dashed black lines) together with its standard deviation (grey shaded area) in metres. The range of variation increases to greater depth. The standard deviation of the velocity is shown for top and bottom of each layer, and it varies between 8% and 42%, with a mean standard deviation of 19%. The velocity deviation also increases to greater depth. The increasing variation with depth can be seen as evidence that there is a decrease in resolution.

To quantify the similarity between the results, we use correlation coefficients and the normalized cross correlation (Fig. 11). Figure 11a shows the normalized cross correlation coefficients for all combinations, with the maximum cross correlation coefficient marked by a black asterisk. The velocity model of the MASW shows only little correlation (0.21) with the velocity model from the time window approach (FWI 2). In contrast, little anticorrelation is observed between the velocity model of the MASW and the velocity model of the sequential frequency approach (FWI 1). The same applies to the correlation with both the conductivity models (Fig. 11b). The value of the maximum normalized cross correlation coefficient between the MASW and FWI velocity models is low (FWI 1: 0.56; FWI 2: 0.47) and accompanied by the highest shifts in x (up to 4.5 m) and z (up to 1.8 m).

Evaluating the performance of the FWI with respect to standard reflection seismic imaging, the resulting velocity model of the time window strategy was compared with the reflection section (Fig. 7). The low-velocity zone at the centre of the magnetic anomaly can be recognized very well in the stacked seismic reflection section. In 0.5 m below the surface, a strong horizontal reflector is seen, which is disrupted around the central magnetic anomaly. Furthermore, there are reflections from the top and bottom of the low-velocity zone. In the deeper part, strong reflections are found where large changes in velocity from high to low and vice versa are observed. The alternating velocity variations in the time window strategy model fit very well with the reflections of the migrated CMP section. Furthermore, the reflection section displays internal layering apparent as several reflections not seen in the velocity model.

Concerning resolution capability, we clearly see the limits as well as the benefits of each applied seismic method. Whereas the MASW may show nominally a horizontal resolution of 0.5 m, it shows only little evidence of the strong lateral velocity contrast associated with the target trench. As typical for surface-wave methods, the vertical resolution decreases proportional to penetration depth. The maximum penetration depth of MASW is about 2.0 m in our case, whereas both the standard reflection seismic imaging and the FWI give
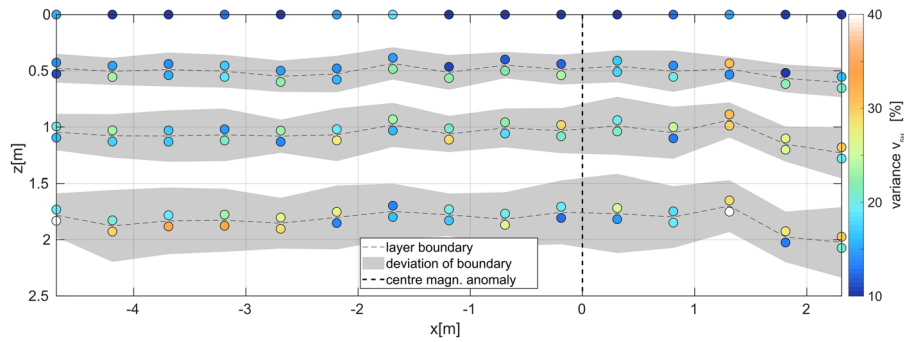
Figure 12 Variances of the depth of layer boundaries and velocity for all 15 centre points along the profile. The layer boundaries are shown as a black dashed line; the variance of the layer boundary depths in m is shown as a grey shaded area. The variance of the velocity in percent is shown as colour-coded circles. The centre of the magnetic anomaly is marked by a dashed black line.

reliable models also of the deeper subsurface. The resolution of the migrated section is about 0.4 m vertically and horizontally with a maximal penetration depth of approximately 6.0 m.

The resolution capability of the applied FWI algorithm regarding Love waves was investigated by previous studies (Dokter, 2015; Dokter *et al.*, 2017), which used the same FWI algorithm and workflow along with a comparable study design as in the present study. They performed checkerboard and other synthetic tests to estimate resolution as a function of the depth. For a background velocity of 220 m/s it turned out Love waves can resolve 1 m scale structures down to 4.0 m depth and 2 m scale structures down to 8.0 m depth. As the mean velocity in our model is lower, the dominant wavelength is shorter, resulting in an increased resolution (mean velocity: 220 m/s compared with 100 m/s). Köhn *et al.* (2019) demonstrated that even smaller than 1 m scale velocity variations could be correlated with structures in an archaeological excavation sketch/photograph. All studies confirm that structures smaller than 1.0 m × 1.0 m can be recognized reliable. The difference between the present study and the previous ones is that our data set contains reflections of considerable amplitude beside the Love waves. Obviously, the reflections are responsible for increasing the FWI resolution to submetre scales down to 8 m depth.

For this study, the very-near-surface sediments of the uppermost 1.5 m are of particular interest, especially the graben-shaped target structure of 0.8 m by 3.0 m. This is in reach of an excavation, which can be used for ground truthing the FWI results. The comparison with the archaeological trench clearly shows that the obtained velocity structure matches the excavated pattern of strata very well. Although the migrated seismic reflection image is also able to map the target, the reflection image is, on the one hand, more difficult to understand because the velocity information is missing. On the

other hand, the reflection image enhances first-order discontinuities visually, which may appear somewhat smoothed in the FWI velocity section. Therefore, combined FWI-reflection sections such as Fig. 7 appear best suited for interpretation.

8.3 Performance of full waveform inversion in comparison with non-seismic methods

As the comparison with the inverted electrical conductivity profiles by ERT and EMI showed, there is some visual similarity between the models. The high-velocity structure of the upper metre maps into a region of low conductivity, whereas high conductivities coincide with lower velocities. The small-scale variations seen in the conductivity model directly below the surface are not seen as clearly in the velocity model. The conductivity models do not show structure that fits well with the pattern of strata found in the excavation. Where the topsoil deepens, the conductivity increases in both models to its maximum.

To quantify the similarity between the results, we take a look at the correlation coefficients and the normalized cross correlation. The correlation coefficients for the trend-corrected data show a high correlation (0.94) between the ERT and EMI conductivity models (Fig. 11b). Furthermore, there is a very good correlation (0.85) between both the conductivity models and the velocity model from the sequential frequency approach (FWI 2). In contrast, weak anticorrelation (−0.5 to −0.6) is observed between the conductivity models and the velocity model of the time window approach (FWI 1).

Again, the normalized cross correlation shows a moderate correlation (0.5 to 0.8) between the conductivity models and the velocity model FWI 2 of the sequential frequency workflow. The spatial pattern shifts are relatively small, about 0.5 m in the vertical direction. These small vertical shifts arise

from the different depth sensitivities of the applied methods and the smoothing included in the inversion. Larger pattern shifts (>1.5 m) are observed between the velocity model of the time window approach and all others. Noteworthy again are the low values of the maximum normalized cross correlation coefficient for the MASW velocity model (0.47–0.56), accompanied by the highest shifts in x (up to 4.5 m) and z (up to 1.8 m).

Based on the ground truthing with excavation and corings, the FWI time window strategy yielded the most detailed and most reliable model of the subsurface with the highest structural resolution compared with the non-seismic methods and the sequential frequency approach. The observed high shift and anticorrelation can be seen as a result of the improved resolution of FWI 1 compared with all other methods.

8.4 Origin and interpretation of the magnetic anomaly

The resulting velocity model together with the analysis of all other applied geophysical methods allows to further discuss the nature of the observed magnetic anomaly. As no archaeological artefacts were found in the corings (Fig. 8) and excavation (Fig. 9), the cause of the anomaly must be due to sedimentological changes. Considering the correlation between seismic velocity and changing sand content (Fig. 9b), the magnetic modelling (Fig. 10) using the low-velocity body from both FWI strategies clarifies that the facies characterized by the low-velocity zone can act as source for the magnetic anomaly. Although the magnetic modelling does not perfectly match the observed data and small deviations occur, the bodies based on the seismic velocity models and the modelled contrasts in susceptibility explain most of the observed anomaly. Deeper structures not considered in the modelling and not observed in the FWI result as well as other small heterogeneities may be the cause of the deviations. As no man-made features like walls were found in the subsurface the difference in susceptibility is probably only caused by variations in the amount of sand and the mineral contents.

Based on the age estimations of coring Ain5, the investigated structure can be transferred to an archaeological context. Coring Ain5 was conducted in the area of the investigated linear magnetic anomaly and is close to Ain26. By levelling the ages to sea level, we are convinced that the sedimentary history of Ain26 is comparable (Brückner *et al.*, 2015). As coring Ain5 yielded ages of cal AD 1416–1665 in a depth of 1.15 m b.s.l. and the base of the graben-like structure is not found deeper than 1.0 m, it is probable that the structure dates in Ottoman or modern times; therefore, no connection

with Thracian Ainos and its potential harbour structures can be expected. The purpose of the observed structure in an archaeological context remains unclear. Literary evidence from the 15th century conveys salt production in Ainos (Reinsch, 1983). The observed structure might have been a small channel to supply evaporative ponds with salty water. It can also not be excluded that the features represent silted up drainage canals in a futile attempt to turn the area into arable land.

9 CONCLUSION

In methodical perspective, the presented results show that the full waveform inversion (FWI) of multi-fold covered SH-wave data is a practicable tool in near-surface archaeological prospecting. It enables not only to image the subsurface with high resolution but also to determine SH-wave velocity as a sediment parameter, on the basis of which further target assessment can be performed. The potential of the applied 2D-SH-FWI algorithm to map and resolve small-scale variations of near-surface sediment changes could be demonstrated by this example. Tests involving ground truthing and comparative geophysical methods showed the important influence of the applied inversion strategy on resolution, where the time window strategy turned out to give more realistic results than the sequential frequency strategy. In resolution, both FWI strategies brought visibly more differentiated results than standard multichannel analysis of surface waves, reflection seismic and geoelectric methods. The latter suffered from the low electrical resistivity values of the swampy environment of the example site.

As to the specific archaeological target, serving as an example in the present study, the structure causing a previously mapped major magnetic anomaly could be identified by FWI. The causative structure turned out to be too shallow for being of Ancient or Early Byzantine age, whereas its urbanistic purpose remains still unclear. It is well possible that these features are remains of medieval or later saltworks, or that they are remains of a futile attempt to drain the area.

the NEC-HPC Linux-Cluster at the computation centre of Kiel University. We like to thank J. Andersen, S. Splettstößer, C. Mohr, E. Erkul, I. Kaplanvural, I. Folkers, and P. Leineweber for their support during fieldwork.

ORCID

Michaela Schwardt [ID]
https://orcid.org/0000-0002-5639-3945

REFERENCES

Aitken, M. (1958) Magnetic prospecting I. *Archaeometry*, 1, 24–29.

Aki, K. and Richards, P. (1980) *Quantitative Seismology*. New York: W.H. Freeman and Company.

Alam, M. (2019) Near-surface characterisation using traveltime and full-waveform inversion with vertical and horizontal component seismic data. *Interpretation*, 7, T141–T154.

Anderson, W. (1989) A hybrid fast Hankel transform algorithm for electromagnetic modeling. *Geophysics*, 54, 263–266.

Anzidei, M., Antonioli, F., Benini, A., Lambeck, K., Sivan, D., Serpelloni, E. *et al.* (2011) Sea level change and vertical land movements since the last two millennia along the coasts of southwestern Turkey and Israel. *Quaternary International*, 232, 13–20.

Başaran, S. (1999) Zum Straßennetz um Ainos. In: (eds P. Scherrer, H. Täuber and H. Thür), *Steine und Wege - Festschrift Dieter Knibbe*, pp. 343–348. Vienna, Austria: Österreichisches Archäologisches Institut.

Başaran, S. (2001) The excavations at Enez (Ainos). In: *İstanbul University's Contributions to Archaeology in Turkey 1932–2000* (ed. O. Belli), pp. 219–226. Istanbul, Turkey: Istanbul University Rectorate Publication No. 4285.

Belshé, J. (1957) Recent magnetic investigations at Cambridge University. *Advances in Physics*, 6, 192–193.

Bevan, B. and Kenyon, J. (1975) Ground-penetrating radar for historical archaeology. *Masca Newsletter*, 11, 2–17.

Bharadwaj, P., Drijkoningen, G., Mulder, W., Thorbecke, J., Neducza, B. and Jenneskens, R. (2017) A shear-wave seismic system using full-waveform inversion to look ahead of a tunnel-boring machine. *Near Surface Geophysics*, 15, 210–224.

Blott, S. and Pye, K. (2001) GRADISTAT: a grain size distribution and statistics package for the analysis of unconsolidated sediment. *Earth Surface Processes and Landforms*, 26, 1237–1248.

Bohlen, T. (2002) Parallel 3-D viscoelastic finite difference seismic modelling. *Computers & Geosciences*, 28, 887–899.

Bohlen, T., Kugler, S., Klein, G. and Theilen, F. (2004) 1.5 D inversion of lateral variation of Scholte-wave dispersion. *Geophysics*, 69, 330–344.

Bonsall, J., Fry, R., Gaffney, C., Armit, I., Beck, A. and Gaffney, V. (2013) Assessment of the CMD Mini-Explorer, a new low-frequency multi-coil electromagnetic device, for archaeological investigations. *Archaeological Prospection*, 20, 219–231.

Boyce, J., Reinhardt, E., Raban, A. and Pozza, M. (2004) Marine magnetic survey of a submerged Roman harbour, Caesarea Maritima, Israel. *International Journal of Nautical Archaeology*, 33, 122–136.

Brückner, H., Schmidts, T., Bücherl, H., Pint, A. and Seeliger, M. (2015) Die Häfen und ufernahen Befestigungen von Ainos – eine Zwischenbilanz. In: (eds T. Schmidts and M. Vučetić), *Häfen im 1. Millennium AD: bauliche Konzepte, herrschaftliche und religiöse Einflüsse, Interdisziplinäre Forschungen zu Häfen von der Römischen Kaiserzeit bis zum Mittelalter in Europa*, Vol. 1 pp. 53–76. Mainz, Germany: Verlag des Römisch-Germanischen Zentralmuseums.

Bunks, C., Saleck, F., Zaleski, S. and Chavent, G. (1995) Multiscale seismic waveform inversion: *Geophysics*, 60, 1457–1473.

Chen, J., Zelt, A. and Jaiswal, P. (2017) Detecting a known near-surface target through application of frequency-dependent travel-time tomography and full-waveform inversion to P- and SH-wave seismic refraction data. *Geophysics*, 82, R1–R17.

Choi, Y. and Alkhalifah, T. (2012) Application of multi-source waveform inversion to marine streamer data using the global correlation norm. *Geophysical Prospecting*, 60, 748–758.

Constable, S., Parker, R. and Constable, C. (1987) Occam's inversion: a practical algorithm for generating smooth models from electromagnetic sounding data. *Geophysics*, 52, 289–300.

Courant, R., Friedrichs, K. and Lewy, H. (1928) Über die partiellen Differenzengleichungen der mathematischen Physik. *Mathematische Annalen*, 100, 32–74.

Courant, R., Friedrichs, K. and Lewy, H. (1967) On the partial difference equations of mathematical physics. *IBM journal of Research and Development*, 11, 215–234.

De Smedt, P., Saey, T., Lehouck, A., Stichelbaut, B., Meerschman, E., Islam, M. *et al.* (2013) Exploring the potential of multi-receiver EMI survey for geoarchaeological prospection: A 90 ha dataset. *Geoderma*, 199, 30–36.

De Smedt, P., Saey, T., Meerschman, E., De Reu, J., De Clercq, W. and Van Meirvenne, M. (2014) Comparing apparent magnetic susceptibility measurements of a multi-receiver EMI sensor with topsoil and profile magnetic susceptibility data over weak magnetic anomalies. *Archaeological Prospection*, 21, 103–112.

Dogan, M. and Papamarinopoulos, S. (2003) Geoelectric prospection of a city wall by multi-electrode resistivity image survey at the prehistoric site of Asea (southern Greece). *Archaeological Prospection*, 10, 241–248.

Dokter, E. (2015) 2D time domain waveform inversion of a near surface SH wave data set from Čachtice, Slovakia. Diploma thesis. Kiel University, Germany.

Dokter, E., Köhn, D., Wilken, D., De Nil, D. and Rabbel, W. (2017) Full waveform inversion of SH-and Love-wave data in near-surface prospecting. *Geophysical Prospecting*, 65, 216–236.

Eberhart, R. and Kennedy, J. (1995) A new optimizer using particle swarm theory. *Proceedings of the Sixth International Symposium on Micro Machine and Human Science*, pp. 39–43.

Engel, M., Knipping, M., Brückner, H., Kiderlen, M. and Kraft, J. (2009) Reconstructing middle to late Holocene palaeogeographies of the lower Messenian plain (southwestern Peloponnese, Greece): coastline migration, vegetation history and sea level change. *Palaeogeography, Palaeoclimatology, Palaeoecology*, 284, 257–270.

Ernst, W. (1970) *Geochemical Facies Analysis*. Elsevier.

Flemming, N. (1978) Holocene eustatic changes and coastal tectonics in the northeast Mediterranean: implications for models of crustal consumption. *Philosophical Transactions of the Royal Society of London. Series A, Mathematical and Physical Sciences*, 289, 405–458.

Folk, R. and Ward, W. (1957) Brazos River bar [Texas]; a study in the significance of grain size parameters. *Journal of Sedimentary Research*, 27, 3–26.

Forbriger, T. (2003) Inversion of shallow-seismic wavefields: I. Wavefield transformation. *Geophysical Journal International*, 153, 719–734.

Forbriger, T., Groos, L. and Schäfer, M. (2014) Line-source simulation for shallow-seismic data. Part 1: Theoretical background. *Geophysical Journal International*, 198, 1387–1404.

Gibson, T. (1986) Magnetic prospection on prehistoric sites in western Canada. *Geophysics*, 51, 553–560.

Goodman, D. and Nishimura, Y. (1993) A ground-radar view of Japanese burial mounds. *Antiquity*, 67, 349–354.

Groos, L. (2013) *2D full waveform inversion of shallow seismic Rayleigh waves*. PhD thesis, Karlsruhe Institute of Technology, Germany.

Groos, L., Schäfer, M., Forbriger, T. and Bohlen, T. (2014) The role of attenuation in 2D full-waveform inversion of shallow-seismic body and Rayleigh waves. *Geophysics*, 79, R247–R261.

Groos, L., Schäfer, M., Forbriger, T. and Bohlen, T. (2017) Application of a complete workflow for 2D elastic full-waveform inversion to recorded shallow-seismic Rayleigh waves. *Geophysics*, 82, R109–R117.

Günther, T., Rücker, C. and Spitzer, K. (2006) Three-dimensional modelling and inversion of DC resistivity data incorporating topography – II. Inversion. *Geophysical Journal International*, 166, 506–517.

Hansen, P. and O'Leary, D. (1993) The use of the L-curve in the regularization of discrete ill-posed problems. *SIAM Journal on Scientific Computing*, 14, 1487–1503.

Keay, S., Earl, G., Hay, S., Kay, S., Ogden, J. and Strutt, K. (2009) The role of integrated survey methods in the assessment of archaeological landscapes: the case of Portus. *Archaeological Prospection*, 16, 154–166.

Köhn, D., De Nil, D., Kurzmann, A., Przebindowska, A. and Bohlen, T. (2012) On the influence of model parametrization in elastic full waveform tomography. *Geophysical Journal International*, 191, 325–345.

Köhn, D., Kurzmann, A., De Nil, D. and Groos, L. (2014) *DENISE – User Manual*, available at https://danielkoehnsite.files.wordpress.com/2019/06/manual_denise.pdf.

Köhn, D., Schwardt, M., Wilken, D., De Nil, D., Wunderlich, T., Rabbel, W. *et al.* (2017) SH-Wellenforminversion in der oberflächennahen Geophysik. *DGG-Kolloquium: Neue Entwicklungen in der Angewandten Seismik*, pp. 21–31. Deutsche Geophysikalische Gesellschaft.

Köhn, D., Wilken, D., De Nil, D., Wunderlich, T., Rabbel, W. and Werther, L. (2018) 2D full waveform inversion applied to a strongly-dispersive Love wave field dataset. 80th EAGE Conference and Exhibition, Porto, Portugal, Extended Abstracts.

Köhn, D., Wilken, D., De Nil, D., Wunderlich, T., Rabbel, W., Werther, L. *et al.* (2019) Comparison of time-domain SH waveform inversion strategies based on sequential low and bandpass filtered data for improved resolution in near-surface prospecting. *Journal of Applied Geophysics*, 160, 69–83.

Komatitsch, D. and Martin, R. (2007) An unsplit convolutional perfectly matched layer improved at grazing incidence for the seismic wave equation. *Geophysics*, 72, SM155–SM167.

Krampe, V., Pan, Y. and Bohlen, T. (2019) Two-dimensional elastic full-waveform inversion of Love waves in shallow vertically transversely isotropic media: synthetic reconstruction tests. *Near Surface Geophysics*, 17, 449–461.

Lange, G. and Jacobs, F. (2005) Gleichstromgeoelektrik. In: (eds K. Knödel, H. Krummel and G. Lange), *Geophysik* pp. 122–165. Berlin: Springer.

Larson, D., Lipo, C. and Ambos, E. (2003) Application of advanced geophysical methods and engineering principles in an emerging scientific archaeology. *First Break*, 21, 51–62.

Leucci, G., Greco, F., De Giorgi, L. and Mauceri, R. (2007) Three-dimensional image of seismic refraction tomography and electrical resistivity tomography survey in the castle of Occhiola (Sicily, Italy). *Journal of Archaeological Science*, 34, 233–242.

Levander, A. (1988) Fourth-order finite-difference P-SV seismograms. *Geophysics*, 53, 1425–1436.

McMechan, G. and Yedlin, M. (1981) Analysis of dispersive waves by wave field transformation. *Geophysics*, 46, 869–874.

Mohamed, A., El-Hussain, I., Deif, A., Araffa, S., Mansour, K. and Al-Rawas, G. (2019) Integrated ground penetrating radar, electrical resistivity tomography and multichannel analysis of surface waves for detecting near-surface caverns at Duqm area, Sultanate of Oman. *Near Surface Geophysics*, 17, 379–401.

Neidel, N. and Tanner, M. (1971) Semblance and other coherency measure for multichannel data. *Geophysics*, 36, 482–497.

Neubauer, W. (2001) Magnetische Prospektion in der Archäologie. Verlag der Österreichischen Akademie der Wissenschaften.

Nguyen, T., Tran, K. and McVay, M. (2016) Evaluation of unknown foundations using surface-based full waveform tomography. *Journal of Bridge Engineering*, 21, 04016013.

Nocedal, J. and Wright, S. (2006) *Numerical Optimization*. New York: Springer.

Oldenburg, D. and Li, Y. (1999) Estimating depth of investigation in dc resistivity and IP surveys. *Geophysics*, 64, 403–416.

Pan, Y., Gao, L. and Bohlen, T. (2017) Sequential phase-velocity and waveform inversion of shallow-seismic surface waves - a field example for Bedrock Mapping. 23rd European Meeting of Environmental and Engineering Geophysics, Extended Abstract.

Paoletti, V., Secomandi, M., Piromallo, M., Giordano, F., Fedi, M. and Rapolla, A. (2005) Magnetic survey at the submerged archaeological site of Baia, Naples, Southern Italy. *Archaeological Prospection*, 12, 51–59.

Papadopoulos, N., Tsourlos, P., Tsokas, G. and Sarris, A. (2006) Two-dimensional and three-dimensional resistivity imaging in archaeological site investigation. *Archaeological Prospection*, 13, 163–181.

Rabbel, W., Erkul, E., Stümpel, H., Wunderlich, T., Pašteka, R., Papco, J. *et al.* (2015b) Discovery of a Byzantine Church in

Iznik/Nicaea, Turkey: an educational case history of geophysical prospecting with combined methods in urban areas. *Archaeological Prospection*, 22, 1–20.

Rabbel, W. and Müller-Karpe, A. (2004) Trecker und Sensoren – Geophysik erforscht antike Siedlungsräume. In: *Alte Fragen – neue Antworten. Neue naturwissenschaftliche Methoden und Technologien in den Geisteswissenschaften*, pp. 102–107. Bundesministerium für Bildung und Forschung.

Rabbel, W., Stümpel, H. and Woelz, S. (2004) Archeological prospecting with magnetic and shear-wave surveys at the ancient city of Miletos (western Turkey). *The Leading Edge*, 23, 690–703.

Rabbel, W., Wilken, D., Wunderlich, T., Bödecker, S., Brückner, H., Byock, J. *et al.* (2015a) Geophysikalische Prospektion von Hafensituationen – Möglichkeiten, Anwendungen und Forschungsbedarf. In: (eds T. Schmidts and M. Vučetić), *Häfen im 1. Millennium AD: bauliche Konzepte, herrschaftliche und religiöse Einflüsse, Interdisziplinäre Forschungen zu Häfen von der Römischen Kaiserzeit bis zum Mittelalter in Europa*, Vol. 1, pp. 323–340. Mainz, Germany: Verlag des Römisch-Germanischen Zentralmuseums.

Ravaut, C., Operto, S., Improta, L., Virieux, J., Herrero, A. and Dell'Aversana, P. (2004) Multiscale imaging of complex structures from multifold wide-aperture seismic data by frequency-domain full-waveform tomography: application to a thrust belt. *Geophysical Journal International*, 159, 1032–1056.

Reinsch, D. (1983) *Critobuli Imbriotae Historiae*. Berlin: Walter de Gruyter.

Rizzo, E., Chianese, D. and Lapenna, V. (2005) Magnetic, GPR and geoelectrical measurements for studying the archaeological site of 'Masseria Nigro' (Viggiano, southern Italy). *Near Surface Geophysics*, 3, 13–19.

Robertsson, J. (1996) A numerical free-surface condition for elastic/viscoelastic finite-difference modelling in the presence of topography. *Geophysics*, 61, 1921–1934.

Schäfer, M. (2014) *Application of full-waveform inversion to shallow-seismic Rayleigh waves on 2D structures*. PhD thesis, Karlsruhe Institute of Technology.

Schön, J. (2015) *Physical Properties of Rocks: Fundamentals and Principles of Petrophysics*. Elsevier.

Seeliger, M., Bartz, M., Erkul, E., Feuser, S., Kelterbaum, D., Klein, C. *et al.* (2013) Taken from the sea, reclaimed by the sea: The fate of the closed harbour of Elaia, the maritime satellite city of Pergamum (Turkey). *Quaternary International*, 312, 70–83.

Seeliger, M., Pint, A., Frenzel, P., Feuser, S., Pirson, F., Riedesel, S. *et al.* (2017) Foraminifera as markers of Holocene sea-level fluctuations and water depths of ancient harbours—a case study from the Bay of Elaia (W Turkey). *Palaeogeography, Palaeoclimatology, Palaeoecology*, 482, 17–29.

Seeliger, M., Pint, A., Frenzel, P., Weisenseel, P., Erkul, E., Wilken, D. *et al.* (2018) Using a multi-proxy approach to detect and date a buried part of the Hellenistic City Wall of Ainos (NW Turkey). *Geosciences*, 8, 357.

Socco, L., Foti, S. and Boiero, D. (2010) Surface-wave analysis for building near-surface velocity models – established approaches and new perspectives. *Geophysics*, 75, A83–A102.

Sponagel, H. (2005) Ad-hoc-Arbeitsgruppe Boden der staatlichen geologischen Dienste und der Bundesanstalt für Geowissenschaften und Rohstoffe Bodenkundliche Kartieranleitung.

Stümpel, H. (1988) Erdradar: Ein neues Prospektionsverfahren in der Archäologie. *Archäologie in Deutschland*, 1, 28–31.

Talwani, M. and Heirtzler, J. (1964) Computation of magnetic anomalies caused by two-dimensional bodies of arbitrary shape. *Computers in the Mineral Industries*, 1, 464–480.

Tarantola, A. (2005) *Inverse Problem Theory and Methods for Model Parameter Estimation*, Vol. 89. Philadelphia: SIAM.

Tran, K. and McVay, M. (2012) Site characterization using Gauss–Newton inversion of 2-D full seismic waveform in the time domain. *Soil Dynamics and Earthquake Engineering*, 43, 16–24.

Tran, K., McVay, M., Faraone, M. and Horhota, D. (2013) Sinkhole detection using 2D full seismic waveform tomography. *Geophysics*, 78, R175–R183.

Tran, K. and Sperry, J. (2018) Application of 2D full-waveform tomography on land-streamer data for assessment of roadway subsidence. *Geophysics*, 83, EN1–EN11.

Vafidis, A., Economou, N., Ganiatsos, Y., Manakou, M., Poulioudis, G., Sourlas, G. *et al.* (2005) Integrated geophysical studies at ancient Itanos (Greece). *Journal of Archaeological Science*, 32, 1023–1036.

Vickers, R. and Dolphin, L. (1975) A communication on an archaeological radar experiment at Chaco Canyon, New Mexico. *MASCA Newsletter*, 11, 3–3.

Virieux, J. (1984) SH-wave propagation in heterogeneous media: Velocity-stress finite-difference method. *Geophysics*, 49, 1933–1942.

Virieux, J. and Operto, S. (2009) An overview of full waveform inversion in exploration geophysics. *Geophysics*, 74, WCC1–WCC26.

von Carnap-Bornheim, C. and Kalmring, S. (2011) DFG-Schwerpunktprogramm 1630. Häfen von der Römischen Kaiserzeit bis zum Mittelalter. Zur Archäologie und Geschichte regionaler und überregionaler Verkehrssysteme. In: *Annual Report Centre for Baltic and Scandinavian Archaeology*, pp. 28–31.

von Ketelhodt, J., Fechner, T., Manzi, M. and Durrheim, R. (2018) Joint inversion of cross-borehile P-waves, horizontally and vertically polarized S-waves: tomographic data for hydro-geophysical site characterization. *Near Surface Geophysics*, 16, 529–542.

Vött, A., Bareth, G., Brückner, H., Lang, F., Sakellariou, D., Hadler, H. *et al.* (2011) Olympia's harbour site Pheia (Elis, western Peloponnese, Greece) destroyed by tsunami impact. *Die Erde*, 142, 259–288.

Wilken, D. and Rabbel, W. (2012) On the application of particle swarm optimization strategies on Scholte-wave inversion. *Geophysical Journal International*, 190, 580–594.

Wilken, D., Wunderlich, T., Andersen, J. and Rabbel, W. (2015a) Geophysical investigation of past harbours: challenges and application examples. *Proceedings of the 11th International Conference on Archaeological Prospection*, 526–527. Warsaw, Poland.

Wilken, D., Wunderlich, T., Majchczack, B., Andersen, J. and Rabbel, W. (2015b) Rayleigh-wave resonance analysis: a methodological test on a Viking Age pit house. *Archaeological Prospection*, 22, 187–206.

Woelz, S. and Rabbel, W. (2005) Seismic prospecting in archaeology: a 3D shear-wave study of the ancient harbour of Miletus (Turkey). *Near Surface Geophysics*, 3, 245–257.

Woelz, S., Rabbel, W. and Mueller, C. (2009) Shear waves in near surface 3D media–SH–wavefield separation, refraction time migration and tomography. *Journal of Applied Geophysics*, 68, 104–116.

Wunderlich, T., Wilken, D., Andersen, J., Rabbel, W., Zori, D., Kalmring, S. *et al.* (2015) On the ability of geophysical methods to image medieval turf buildings in Iceland. *Archaeological Prospection*, 22, 171–186.

Wunderlich, T., Wilken, D., Erkul, E., Rabbel, W., Vött, A., Fischer, P. *et al.* (2018) The river harbour of Ostia Antica-stratigraphy, extent and harbour infrastructure from combined geophysical measurements and drillings. *Quaternary International*, 473, 55–65.

Yang, P., Brossier, R., Métivier, L. and Virieux, J. (2016) A review on the systematic formulation of 3-D multiparameter full waveform inversion in viscoelastic medium. *Geophysical Journal International*, 207, 129–149.

Zhang, F., Lui, B., Lui, L., Wang, J., Lin, C., Yang, L. *et al.* (2019) Application of ground penetrating radar to detect tunnel lining defects based on improved full waveform inversion and reverse time migration. *Near Surface Geophysics*, 17, 127–139.

Zhang, Z., Huang, L. and Lin, Y. (2012) Double-difference elastic-waveform inversion with weighted gradients for monitoring EGS reservoirs. In *Thirty-Seventh Workshop on Geothermal Reservoir Engineering*. Stanford, California: Stanford University.

APPENDIX A: PARAMETERS AND SPECIFICATIONS OF THE APPLIED METHODS

Table A.1 Parameters, specifications and details of applied geophysical methods

	Profile length	Equipment	Spacing	Sampling rate/sampling interval	Positioning	Other
Magnetics	–	6 Foerster fluxgate differential vertical component magnetometers	Internal: 0.65 m Horizontal: 0.5 m	20 Hz	RTK-DGPS (Leica 530)	–
GPR	–	1 channel SIR 3000 (GSSI); 200 MHz and 400 MHz antennas (GSSI)	–	–	RTK-DGPS (Leica 530)	–
ERT	15.75 m	64 electrodes; RESECS II (Geoserve)	Electrode spacing: 0.25 m		RTK-DGPS (Leica 530; first and last electrode)	Electrode configuration: Wenner-alpha and dipole–dipole
EMI	1 profile, 20 m	CMD MiniExplorer (GF Instruments)	1.0 m point spacing	0.1 s	RTK-DGPS (Leica 530; first and last point)	Internal coil spacing: 0.32 m, 0.71 m, 1.18 m
Seismics	11.75 m	48 10-Hz horizontal geophones; Geometrix Geode seismograph	Geophones: 0.25 m Shotpoints: 0.25 m (located midway between 2 receivers)	0.125 ms	RTK-DGPS (Leica 530; first and last point)	Recording time: 0.5 s

Table A.2 Information on physical parameters, petrophysical links, resolution and depth of penetration as well as respective noise levels and errors in each applied method

| | *Magnetics* | *ERT* | *EMI* | *Seismic* | | |
				Conventional	*MASW*	*FWI*
Physical parameter (geophysical observable)	Magnetic susceptibility	Electrical conductivity	Electrical conductivity	Propagation velocity, elastic properties		
Advantages	Fast, large areas	Depth resolution	Fast	Greater depth of investigation, not relying on contrast in electrical parameters	Velocity models	
Disadvantages	No depth resolution	Slow, single profiles	No real depth resolution	Slow, single profiles, longer processing/computation times		
Petrophysical links	Content of magnetic minerals, chemical composition, sedimentation conditions, grain size	Porosity, pore fluids, water saturation, clay content	Porosity, pore fluids, water saturation, clay content, magnetic properties	Porosity, grain size, mineral content, compaction, density		
Resolution	In-line: 0.05 m crossline: 0.5 m	Horizontal: 0.25 m	Horizontal: 1.0 m	0.4 m	0.5 m	< 1.0 m
Penetration depth	–	0.8 m (dipole–dipole) 2.6 m (Wenner)	~2.4 m	> 6.0 m	~ 1.0 m	> 6.0 m
Noise level/errors	–	< 5 %	< 1 %	offset < 3.25 m: S/N>30 3.25 m < offset > 9.0 m: S/N~12 offset>11.0 m: S/N<5		
Model RMS	Modelling: 2.3/2.4 nT	5.4 %	3.8 %	–	–	–

Table A.3 Parameters for magnetic modelling

Direction of magnetization	Inclination Earth magnetic field (°)	59.01
	Declination Earth magnetic field (°)	4.75
	Azimuth (°)	51.54
	Magnetic Induction (nT)	47387.2
Magnetometer	Inclination (°)	90
	Declination (°)	0
	Azimuth (°)	0
	Height above ground (m)	0.2
	Internal sensor spacing (m)	0.6

Table A.4 Parameters, specifications and details of applied geological, archaeological and geoarchaeological methods

Method	Equipment	Software	Other
Coring	Atlas Copco Cobra TT vibracorer	–	Maximal depth 5.0 m b.s. (below surface)
Grain-size analysis	Beckman Coulter LS13320	GRADISTAT (Blott and Pye, 2001)	–
XRF spectrometry	Niton Xl3t 900 GOLDD (Vött *et al.*, 2011)	–	Ball triturator (Retsch PM 4001)
XRD	Siemens D5000	DiffracPlus Eva software package (Bruker AXS, Berlin, Germany).	–

APPENDIX B: MULTICHANNEL ANALYSIS OF SURFACE WAVES

Table B.1 Parameters used for particle swarm optimization

hmin (m)	*hmax* (m)	V_{SH} (m/s)	Dv_{SH} (m/s)
0.2	0.8	60	40
0.3	0.8	100	60
0.5	1.0	80	40
1.5	1.5	120	80

Local wavefields $\mathbf{A}_{\mathrm{local}}(x,t)$ are extracted from the trace-normalized and spreading corrected data $\mathbf{A}(x,t)$ of the first shot ($x_s = 0$ m) at moving centre points x_c with evenly spaced offsets (0.5 m distance, starting at 2.5 m and ending at 9.5 m) and multiplied by a Gaussian amplitude window with a half-width H of 3.0 m (eq. (B.1)),

$$\mathbf{A}_{\mathrm{local}}(x, t) = \mathbf{A}(x, t)\, e^{\frac{-\left(x-x_c\right)^2}{H/2}}. \tag{B.1}$$

The multiplication with a Gaussian amplitude window helps to avoid model side-lobes (Forbriger, 2003). Using the slant-stack procedure by McMechan and Yedlin (1981), the obtained local wavefields are then transformed from the offset-time domain to the frequency-slowness domain to retrieve phase-slowness frequency (*p–f*) spectra (Fig. B.1):

$$\mathbf{A}_{\mathrm{local}}(p, f) = \sum_{n=1}^{N} \tilde{\mathbf{A}}(x_n, f)\, e^{-2\pi f p x_n}, \tag{B.2}$$

where $\tilde{\mathbf{A}}$ denotes the Fourier transform of the local wavefield, N denotes the number of geophones, and x_n denote the discrete offset positions. The spectra show dispersion curves of four excited Love-wave modes, which are identified for each position x_c and fitted with modelled dispersion curves. We use the adapted Particle Swarm Optimization of Wilken and Rabbel (2012) to minimize the misfit between observed and modelled dispersion curves, resulting in 1D shear-wave velocity models for each offset position x_c.

The particle swarm optimization (PSO) approach is a global stochastic search algorithm and was introduced by Eberhart and Kennedy (1995). A randomly created swarm of particles, which represents vectors in the parameter space is the basis of this approach. The misfit of the swarm is evaluated, the best positions of each particle as well as the globally best position are determined. Then, a displacement vector is assigned to each particle, realizing the movement of a particle and being the update for the next iteration step. The algorithm uses a weighted sum of the slowness-residuals (L1-norm) as misfit function, which will be minimized by the swarm optimization.

We choose to optimize for a model consisting of three layers over a half-space using a swarm size of 300 with 1000 iterations. After 25 unsuccessful iterations, the swarm is reset. Variables to be considered during inversion are shear-wave velocity and layer thickness, whereas density and the quality factor Q_{SH} are kept constant during the inversion. Q_{SH} and the density are set to the same values as during the FWI ($Q_{SH} = 10$, $\rho = 1800$ kg/m³). The initial model and search area, that is the allowed layer depths (*hmin*, *hmax*) and thicknesses along with their velocities variations (v_{SH}, dv_{SH}), were chosen based on the FWI model and the results of the archaeological excavation; the values are stated in Table B.1.

Apart from the search area, the swarm size and the maximum number of iterations, three weighting constants need to be defined to optimize the exploration and convergence in the optimization scheme, namely the weights of initial momentum (0.5), the weight of individual best (0.9) and the weight of global best (0.5).

A statistical analysis was used to find an expected model as well as calculate the model's parameter variances at each offset position x_c.
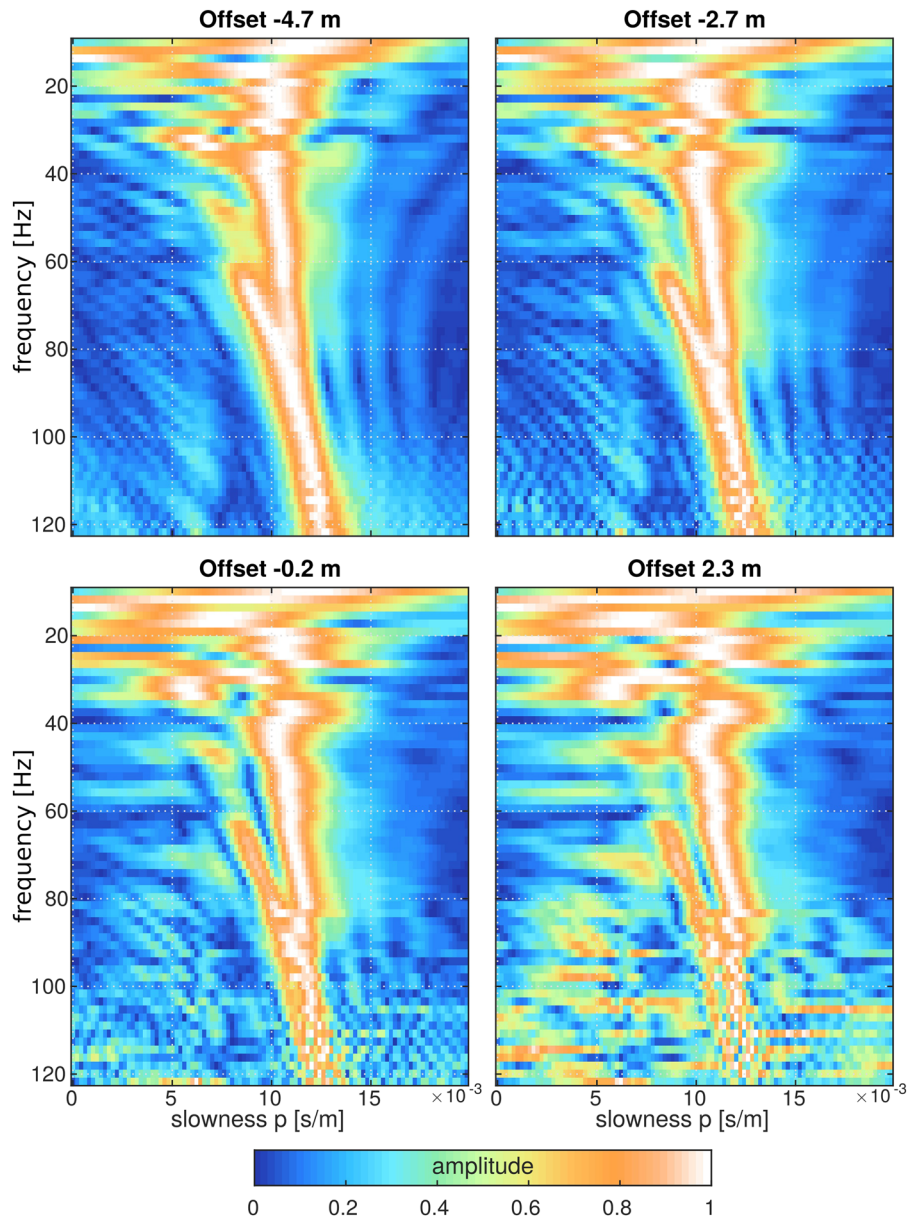
Figure B.1 Local frequency-slowness spectra for four exemplary offsets (−4.7, −2.7, −0.2 and 2.3 m). The spectrum seen in the bottom left is closest to the observed magnetic anomaly minimum. Blue colours denote low and orange colours denote high amplitudes
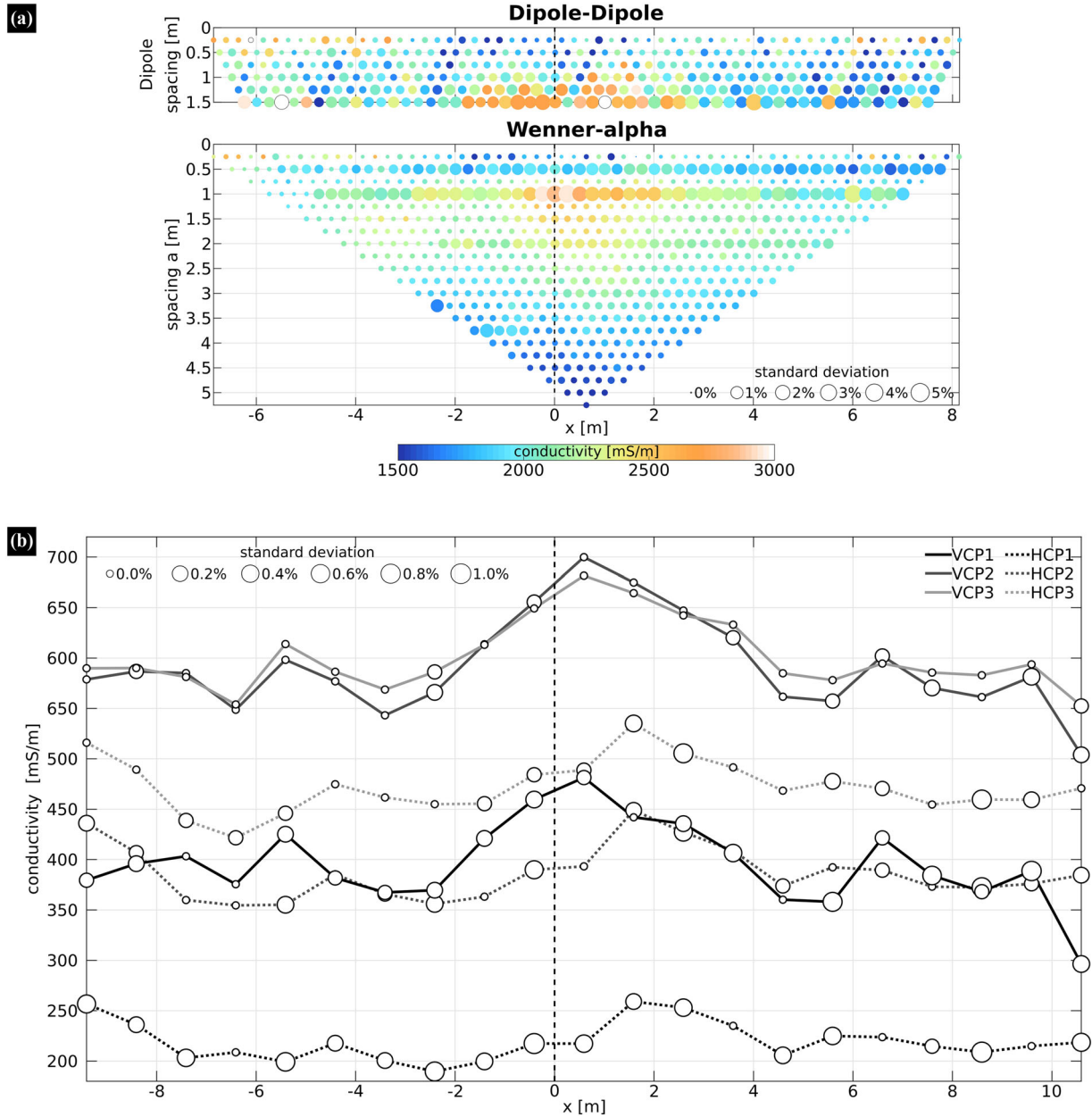
APPENDIX C: EXAMPLES OF RAW DATA

Figure C.1 Raw data for ERT (a) and EMI (b). (a) Acquired pseudosections of the ERT profile for both dipole–dipole and Wenner-alpha configurations. Colours show the measured conductivity values; the standard deviation of each data point is given by the point size. (b) Measured conductivities of the EMI profiles for both the HCP (dotted lines) and VCP (solid lines) modes for all three applied coil distances (black: 0.32 m; dark grey: 0.71 m; light grey: 1.18 m). The standard deviation of each measured point is shown by the point size.

APPENDIX D: DESCRIPTIONS OF INVERSION WORKFLOWS AND MODEL PARAMETRIZATIONS

D.1 Electromagnetic induction

We performed a conductivity inversion using the IX1Dv3 software by Interpex. The profile was inverted using a homogeneous initial model [2040 mS/m, based on the initial model for electric resistivity tomography (ERT)] using the *smooth model estimation* option with Occam's inversion (Constable *et al.*, 1987).

Along the profile, the software inverts each sounding separately. IX1D uses the full Fourier–Hankel transform (Anderson, 1989) in forward modelling to calculate the quadrature component from the field of the specified model, which is then converted to apparent conductivities. Using Occam's inversion, the data are fitted minimizing the least-square error while also minimizing the model's roughness, therefore producing a smooth result. The nonlinear forward problem is linearized about an initial model and then solved for a desired model rather than for a model correction (Constable *et al.*, 1987). The model is parameterized in terms of its first- or second-order derivative with depth. The inversion algorithm searches for the smoothest model possible fitting the data within a tolerance instead of only minimizing the data fit, which would result in a rough model (Constable *et al.*, 1987). For the *smooth model estimation*, all layer thicknesses are kept fixed and only the conductivities are adjusted to fit the data. We choose to invert for ten logarithmically equidistant spaced depth layers with a minimum and maximum layer depth of 0.1 and 3.0 m, respectively, according to the estimated skin depth.

D.2 Electric resistivity tomography

The inversion of the data was carried out using the software package BERT (boundless electrical resistivity tomography; Günther *et al.*, 2006). A homogeneous model of 0.5 Ωm, which corresponds to a mean value of all measured points in the pseudosection, was used as initial model for the inversion of ERT data. As no previous information about the subsurface was known, we used a triangular mesh, with smaller triangles at the top and larger ones at the bottom to represent the decreasing sensitivity with depth. The software uses a Gauss–Newton method with inexact line search to fit the data and applies a global regularization scheme with smoothness constraints to stabilize the solution. A regularization parameter of $\lambda = 54$ was applied in the inversion, which was selected based on the L-curve method (Hansen and O'Leary, 1993), compromising model roughness and data misfit. The inverse problem is solved using a least-squares solver.

D.3 Magnetic modelling

For two alternative subsurface structures with polygonal cross sections derived from the seismic models, we determined the susceptibility contrasts by modelling according to the method of Talwani and Heirtzler (1964).

The direction of magnetization J is calculated with the inclination I, declination D and azimuth C of the Earth magnetic field at the location along with the magnetic induction B (eq. (D.1)).

$$J = \kappa \cdot B,$$
$$J_x = |J| \cdot \cos(I) \cdot \cos(C - D), \tag{D.1}$$
$$J_z = |J| \cdot \sin(I),$$

with J_x and J_z being the components of J and κ being the susceptibility. From that, we can calculate the horizontal, vertical and total components (H, V, T) measured by the magnetometer:

$$V = 2(J_x Q - J_z P),$$
$$H = 2(J_x P + J_z Q), \tag{D.2}$$
$$T = V \sin(I) + H \cos(I) \cos(C - D),$$

where Q and P are calculated for each point along the profile as sum over all corner points of the polygonal body.

For gradiometric measurements, the vertical components of the total fields of both upper and lower sensors are calculated and then subtracted from each other to obtain the modelled anomaly. The only unknown in this calculation is the susceptibility contrast between the subsurface and the structure, which has to be estimated by optimization. As an optimization tool the particle swarm method (PSO) was used. The PSO is a global searching optimization for multimodal problems and uses a randomly created swarm of individuals or parameter vectors, the so-called particles. The particles move and alter their movement for each iteration step to find a desirable position in the parameter space. The parameter space is susceptibility and the background is set to 10^{-5} SI. A swarm of 30 random susceptibility values is generated from which the anomaly is obtained. The misfit between the observed and modelled gradiometric profiles is computed, and the global minimum is searched for 500 iterations, with the swarm being reset after 25 unsuccessful iterations. Furthermore, three weighting constants need to be defined to optimize the exploration and convergence in the optimization scheme, namely

the weights of initial momentum (0.5), the weight of individual best (0.9) and the weight of global best (0.2).

APPENDIX E: BASIC CONCEPT OF FULL WAVEFORM INVERSION

The propagation of elastic waves in a general elastic medium can be described by a system of coupled linear partial differential equations, which consist of the equations of motion:

$$\rho \frac{\partial v_i}{\partial t} = \frac{\partial \sigma_{ij}}{\partial x_j} + f_i, \tag{E.1}$$

where v_i denotes the particle velocity vector, t denotes the time, σ_{ij} denote the stress tensor components, x_j denote the components of the distance vector, and f_i the body force vector. For clarity, the Einstein notation is used, where repeated indices are assumed as summation. Additional equations are introduced to describe how the medium reacts when a force is applied. In the isotropic case, the relation between stress and strain is linear:

$$\sigma_{ij} = \lambda \theta \delta_{ij} + 2\mu \epsilon_{ij},$$
$$\epsilon_{ij} = \frac{1}{2} \left(\frac{\partial u_i}{\partial x_j} + \frac{\partial u_j}{\partial x_i} \right), \tag{E.2}$$

with λ, μ being the Lamé parameters, ε_{ij} the strain tensor, and u_i the displacement. δ_{ij} is the Kronecker's delta and θ describes the cubic dilatation (Aki and Richards, 1980).

The propagation of SH and Love waves assumes only non-zero particle displacements in the y-direction perpendicular to the x–z plane. The underlying forward problem (eq. (E.1)) simplifies to

$$\rho \frac{\partial v_y}{\partial t} = \frac{\partial \sigma_{xy}}{\partial x} + \frac{\partial \sigma_{yz}}{\partial z} + f_y,$$
$$\frac{\partial \sigma_{xy}}{\partial t} = \mu \left(\frac{\partial v_y}{\partial x} \right), \tag{E.3}$$
$$\frac{\partial \sigma_{yz}}{\partial t} = \mu \left(\frac{\partial v_y}{\partial z} \right).$$

Here, v_y denotes the particle velocity component in the y-direction, σ_{xy}, σ_{yz} are shear stresses, and f_y is the body force in the y-direction. The boundary condition at the free surface is given as $\sigma_{yz} = 0$, as required by Love-wave modelling (Köhn *et al.*, 2014; Dokter *et al.*, 2017).

The numerical solution of equation (E.3) is the core of the applied FWI code. To obtain the numerical solution, these equations have to be discretized in time and space on a 2D Cartesian grid. We use a time-domain finite difference (FD) scheme with second-order operators in time and space on a staggered grid (Virieux, 1984; Levander, 1988; Dokter *et al.*,

2017). Numerical instabilities are avoided by satisfying temporal and spatial conditions for the wavefield. The spatial discretization should suffice the grid dispersion criterion to correctly sample the wavefield:

$$dh \le \frac{\lambda_{\min}}{n} = \frac{v_{\min}}{n f_{\max}}, \tag{E.4}$$

with dh being the grid point spacing, $\lambda_{\min}$ and $v_{\min}$ being the minimum wavelength and velocity in the model, respectively, and $f_{\max}$ the maximum frequency of the source signal. Parameter n is dependent on the accuracy of the FD operator, for a second-order operator, it is $n = 12$ (Köhn *et al.*, 2014).

To ensure temporal stability, the Courant criterion has to be satisfied (Courant *et al.*, 1928; Courant *et al.*, 1967). The timestep dt has to be less than the time for the wave to travel between two adjacent grid points with spacing dh:

$$dt \le \frac{dh}{v_{\max} h \sqrt{2}}, \tag{E.5}$$

where $v_{\max}$ is the maximum velocity in the model. The parameter h is again dependent on the FD operator, in the case of a second-order operator, it is $h = 1$ (Köhn *et al.* 2014).

Initial and boundary conditions have to be satisfied in order to find a unique solution. At the top boundary, the free-surface boundary condition required for accurate Love-wave modelling is realized by the image technique (Levander, 1988; Robertsson, 1996; Groos, 2013). The other boundary conditions are realized using convolutional perfectly matched layers (C-PML) absorbing boundary conditions (Komatitsch and Martin, 2007), which damp the waves in an effective way near the boundaries and thus decreasing the FD grid size and saving computational resources compared with an absorbing boundary frame (Köhn *et al.*, 2014; Dokter *et al.*, 2017).

The FWI tries to find an optimum model that explains the measured wavefield best by minimizing the misfit between measured and modelled data. This process is formulated as an iterative optimization problem. This optimization problem is highly nonlinear; therefore, the optimum objective function E needs to be chosen. A trace-normalized objective function, the global correlation norm (GCN; Choi and Alkhalifah, 2012; eq. (E.6)) has been proven to be successful as the seismic phase information is higher weighted than the amplitude information; therefore, it is more robust against variations of amplitudes induced by insufficient source/receiver coupling (Dokter *et al.*, 2017):

$$E = -\sum_{i=1}^{ns} \int_0^T dt \sum_{j=1}^{nr} \left[\frac{u_{ij}^{\mathrm{mod}}(t) \, u_{ij}^{\mathrm{obs}}(t)}{\| u_{ij}^{\mathrm{mod}}(t) \|_2 \| u_{ij}^{\mathrm{obs}}(t) \|_2} \right], \tag{E.6}$$

where *ns* and *nr* are the number of sources and receivers and *T* is the recording time. u_{ij}^{mod} and u_{ij}^{obs} are the modelled and measured data, respectively. In addition, all traces are shifted to a similar energy level as each trace of both the modelled and field data is normalized to its maximum absolute amplitude (Dokter *et al.*, 2017), which attenuates the effect of a non-ideal source/receiver coupling in the acquisition geometry. Furthermore, the use of the global correlation norm as an objective function compensates the difference between the geometric spreading of the surface waves in the 3D real medium as opposed to the 2D model (Dokter *et al.*, 2017). The GCN reduces the sensitivity of the misfit to amplitude errors, allowing for an enhanced performance of the inversion (Choi and Alkhalifah, 2012). The value of the objective function is minimized by updating the model parameters m_n (e.g. SH-wave velocity) iteratively beginning with a starting point in the parameter space, the initial model m_0. The model parameters are updated along a search direction δm_n with a step length μ_n using a preconditioned conjugate gradient method (Nocedal and Wright, 2006):

$$m_{n+1} = m_n + \mu_n \delta m_n,$$
$$\delta m_n = -H_n^{-1}\left(\frac{\partial E}{\partial m}\right)_n, \tag{E.7}$$

where H_n^{-1} denotes the inverse Hessian matrix and $\partial E/\partial m$ denotes the gradient.

The step length μ_n is estimated using an inexact parabolic line search (Nocedal and Wright, 2006). The time-domain gradients of the objective function *E* with respect to the model parameter *m* are calculated using the adjoint-state method (e.g. Tarantola, 2005; Köhn *et al.*, 2012). The gradient for v_s is given by

$$\frac{\partial E}{\partial v_s} = \frac{-2}{v_s^3 \rho} \sum_{i=1}^{ns} \int_0^T \mathrm{d}t \left(\sigma_{xy}\hat{\sigma}_{xy} + \sigma_{yz}\hat{\sigma}_{yz}\right), \tag{E.8}$$

σ_{ii} and v_s are the shear stresses and particle velocity of the forward wavefield, whereas $\hat{\sigma}_{ii}$ are the shear stresses of the adjoint wavefield (Choi and Alkhalifah, 2012).

As the explicit calculation of the Hessian in the time domain requires high computational costs, the diagonal elements of the Hessian are approximated similar to Zhang *et al.* (2012):

$$\tilde{H}_n^{-1} = \left(\lambda_P(x_s) + \sqrt{W_s(x,x_s)\,W_r(x,x_s)}\right)^{-1},$$
$$\lambda_P(x_s) = \epsilon_P \max_x\left\{\sqrt{W_s(x,x_s)\,W_r(x,x_s)}\right\}, \tag{E.9}$$

where $W_s(x,x_s)$ and $W_r(x,x_s)$ define the seismic energies of the forward and adjoint wavefields, excited at source and receiver points x_s and x_r, respectively. To avoid the occurrence of small-scale artefacts below the FWI resolution limit, a smoothing of the gradients is advisable. Similar to Ravaut *et al.* (2004), we apply a Gaussian filter with a correlation length adapted to a fraction of the minimum SH wavelength to the gradient. In this study, all features below approximately a quarter of the dominant SH wavelength are smoothed.

At each iteration step *n*, synthetic data u_{mod} are generated for the current model m_n through forward modelling. During the forward modelling, the unknown source wavelet is estimated for each shot using only near-offset traces with source–receiver distances less than 2.2 m according to the approach of Groos (2013) and Groos *et al.* (2014), where the source wavelet estimation can be described as a linearly damped, least-squares optimization problem. This is done by a stabilized Wiener deconvolution of the recorded seismograms with the simulated seismogram in the frequency domain (Köhn *et al.*, 2014). Moreover, the residuals, gradients and value of the objective function are calculated during each iteration. The iterative process is stopped if the value of the objective function *E* is smaller than a given threshold, or the line search algorithm is not able to find a reasonable large step length.

To account for viscoelastic effects on the amplitude and dispersion of the SH and Love wavefields, a passive homogeneous half-space model for the quality factor Q_s is introduced during forward/adjoint modelling according to Dokter *et al.* (2017). This is done by implementing a generalized standard linear solid composed of four relaxation mechanisms (Bohlen, 2002; Yang *et al.*, 2016).